Article

Tunable strongly coupled superconductivity in magic-angle twisted trilayer graphene

https://doi.org/10.1038/s41586-021-03192-0

Received: 26 October 2020

Accepted: 5 January 2021

Published online: 1 February 2021

Check for updates

Jeong Min Park[1,4], Yuan Cao[1,4]✉, Kenji Watanabe[2], Takashi Taniguchi[3] & Pablo Jarillo-Herrero[1]✉

Moiré superlattices[1,2] have recently emerged as a platform upon which correlated physics and superconductivity can be studied with unprecedented tunability[3–6]. Although correlated effects have been observed in several other moiré systems[7–17], magic-angle twisted bilayer graphene remains the only one in which robust superconductivity has been reproducibly measured[4–6]. Here we realize a moiré superconductor in magic-angle twisted trilayer graphene (MATTG)[18], which has better tunability of its electronic structure and superconducting properties than magic-angle twisted bilayer graphene. Measurements of the Hall effect and quantum oscillations as a function of density and electric field enable us to determine the tunable phase boundaries of the system in the normal metallic state. Zero-magnetic-field resistivity measurements reveal that the existence of superconductivity is intimately connected to the broken-symmetry phase that emerges from two carriers per moiré unit cell. We find that the superconducting phase is suppressed and bounded at the Van Hove singularities that partially surround the broken-symmetry phase, which is difficult to reconcile with weak-coupling Bardeen–Cooper–Schrieffer theory. Moreover, the extensive in situ tunability of our system allows us to reach the ultrastrong-coupling regime, characterized by a Ginzburg–Landau coherence length that reaches the average inter-particle distance, and very large T_{BKT}/T_F values, in excess of 0.1 (where T_{BKT} and T_F are the Berezinskii–Kosterlitz–Thouless transition and Fermi temperatures, respectively). These observations suggest that MATTG can be electrically tuned close to the crossover to a two-dimensional Bose–Einstein condensate. Our results establish a family of tunable moiré superconductors that have the potential to revolutionize our fundamental understanding of and the applications for strongly coupled superconductivity.

When two or more layers of two-dimensional (2D) materials are stacked together, a moiré superlattice with reduced electronic bandwidth can arise from a small twist angle or lattice mismatch between the layers. In such flat-band systems, electronic interactions have a dominant role, which has led to the observation of various correlated and topological phases[3–17,19–23]. The case of magic-angle twisted bilayer graphene (MATBG) has attracted particular attention because of the intriguing superconducting phase it hosts[4–6]. Although signatures of superconductivity have also been reported in other systems[8,9,11,13,17,22,23], definitive evidence of superconductivity—encompassing the observation of zero resistance, sharply switching voltage–current (V–I) characteristics, and Josephson phase coherence—has only been reproducibly demonstrated in MATBG so far.

In this Article, we report the realization of ultrastrong-coupling superconductivity in a magic-angle system that consists of three adjacent graphene layers sequentially twisted by θ and $-\theta$ (Fig. 1a)[18]. Here we consider ultrastrong coupling to exist where $T_c/T_F \gtrsim 0.1$, where T_c is the critical temperature and $T_F = \pi\hbar n^*/(m^* k_B)$ is the Fermi temperature (k_B, Boltzmann constant; $\hbar$, reduced Planck constant; m^*, measured effective mass). This moiré superconductor—magic-angle twisted trilayer graphene (MATTG)—exhibits a rich phase diagram and greater electric field tunability than MATBG. The latter enables us to explore the interplay between correlated states and superconductivity beyond MATBG. Figure 1b, c shows the calculated bandstructures of MATTG without and with an electric displacement field, D (Methods and Extended Data Fig. 1). At zero D, MATTG has a set of flat bands, as well as gapless Dirac bands[18,24–26]. The flat bands in MATTG can be mathematically reduced to MATBG-like bands with an effective twist angle of $\theta/\sqrt{2} \approx \theta/1.4$, and hybridization with the Dirac bands is prohibited by the mirror symmetry[18,25,26]. This reduction leads to a larger magic angle in MATTG, $\theta_{MATTG} \approx 1.6°$. When the mirror symmetry is broken by the application of D, the flat bands can hybridize with the Dirac bands (Fig. 1c), enabling us to control the bandwidth and interaction strength in the flat bands.

[1]Department of Physics, Massachusetts Institute of Technology, Cambridge, MA, USA. [2]Research Center for Functional Materials, National Institute for Materials Science, Tsukuba, Japan. [3]International Center for Materials Nanoarchitectonics, National Institute for Materials Science, Tsukuba, Japan. [4]These authors contributed equally: Jeong Min Park, Yuan Cao. ✉e-mail: caoyuan@mit.edu; pjarillo@mit.edu

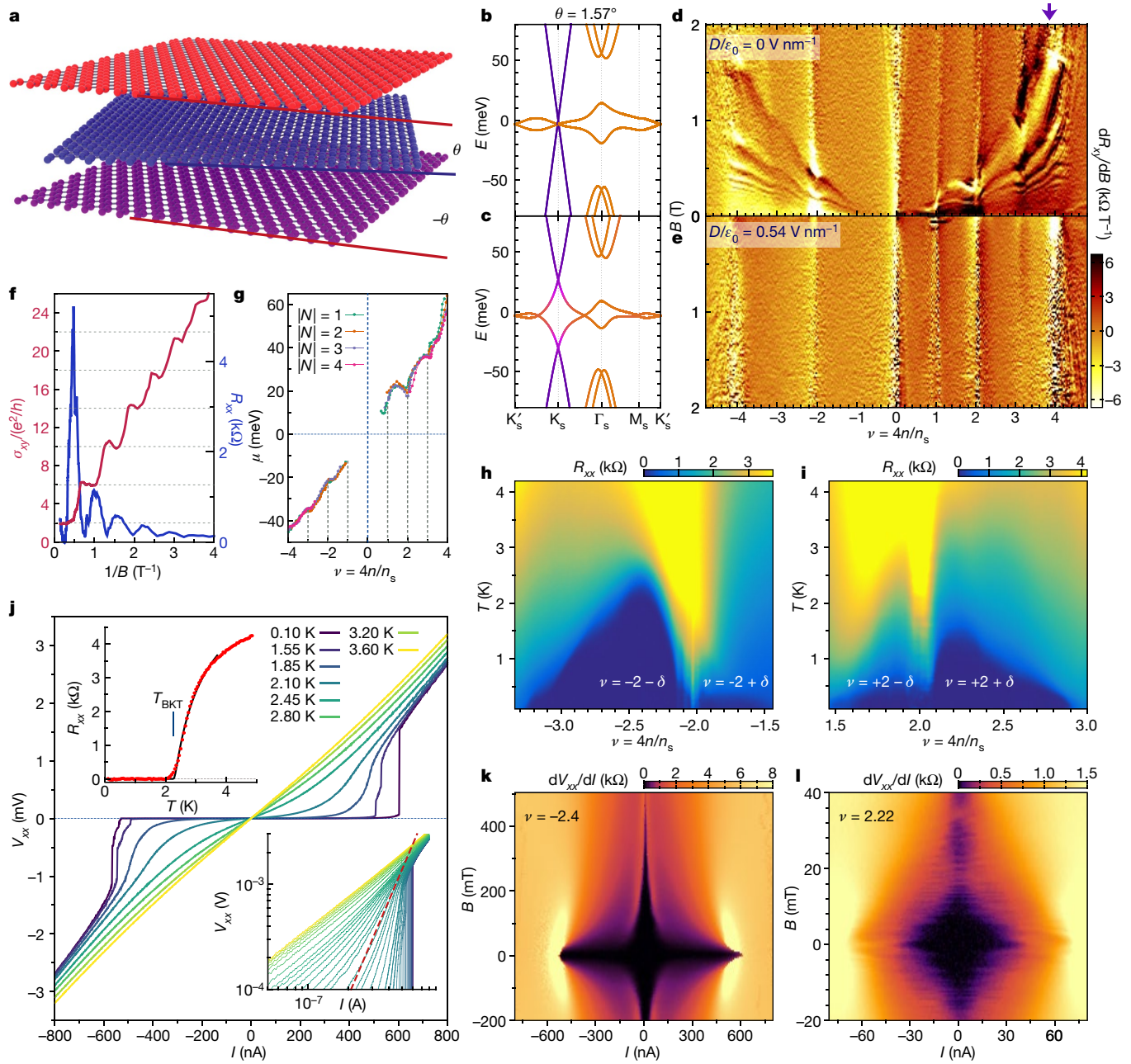

Fig. 1 | Electronic structure and robust superconductivity in mirror-symmetric MATTG. a, MATTG consists of three graphene monolayers stacked in a symmetric arrangement (by rotating with angles θ and $-\theta$ sequentially between the layers). **b**, **c**, Calculated bandstructure of MATTG at zero (**b**) and finite (**c**) perpendicular electric displacement field $D/\varepsilon_0 = 0.2$ V nm^{-1} for valley K (bands for valley K′ can be obtained by time-reversal symmetry), showing flat bands and Dirac bands near the charge-neutrality point. The colour represents the mirror-symmetry character of the eigenstates, which varies from purple (symmetric) to orange (antisymmetric; see Methods). Finite D lifts the mirror symmetry and hybridizes the flat bands and Dirac bands. **d**, **e**, Magnetotransport data (derivative of the Hall resistance R_{xy} with respect to B) of MATTG at $D/\varepsilon_0 = 0$ V nm^{-1} and $D/\varepsilon_0 = 0.54$ V nm^{-1}, respectively. At $D = 0$, we observe extra Landau levels, demonstrating the presence of coexisting Dirac bands, which are lifted by the displacement field. **f**, Longitudinal resistance R_{xx} and Hall conductivity σ_{xy} as a function of inverse magnetic field $1/B$, at moiré filling factor $\nu \lesssim 4$ as marked by the purple arrow above **d**. The quantization of σ_{xy} at 2, 6, 10, ..., e^2/h (h, Planck constant) indicates the presence of the massless Dirac bands. **g**, Estimated chemical potential as a function of ν, extracted from the evolution of Dirac band Landau levels (see Methods), showing a pinning behaviour at all integer fillings. **h**, **i**, R_{xx} versus T and ν showing the superconducting regions near $\nu = -2$ and $\nu = +2$, at $D/\varepsilon_0 = -0.44$ V nm^{-1} and $D/\varepsilon_0 = 0.74$ V nm^{-1}, respectively. **j**, V_{xx}–I curves as a function of temperature at optimal doping in the $\nu = -2 - \delta$ dome. The top-left inset shows a fit of R_{xx}–T data with the Halperin–Nelson formula[30] $R \propto \exp[-b/(T - T_{BKT})^{1/2}]$, where b and T_{BKT} are fitting parameters, which gives $T_{BKT} \approx 2.25$ K. The bottom-right inset shows the V_{xx}–I curves on a log–log scale and sampled at finer temperature increments, again between 0 and 3.6 K, and the dashed line denotes where its slope is approximately 3 ($V_{xx} \propto I^3$), indicating $T_{BKT} \approx 2.1$ K. **k**, **l**, Critical current versus magnetic field at $\nu = -2.4$ (**k**) and $\nu = +2.22$ (**l**), both at $D/\varepsilon_0 = -0.44$ V nm^{-1}. In **k**, the critical current shows a long tail up to 400 mT, whereas **l** shows a clear Josephson interference pattern.

Robust superconductivity in MATTG

We have fabricated three MATTG devices, all of which exhibit robust superconductivity (Methods and Extended Data Fig. 2, 3). Here we focus on the device with a twist angle $\theta = 1.57 \pm 0.02°$—that is, particularly close to θ_{MATTG}. The coexistence of Dirac bands and flat bands in MATTG can be directly observed in the transport data under a perpendicular magnetic field B (Fig. 1d, e). Resistive states at integer fillings of the

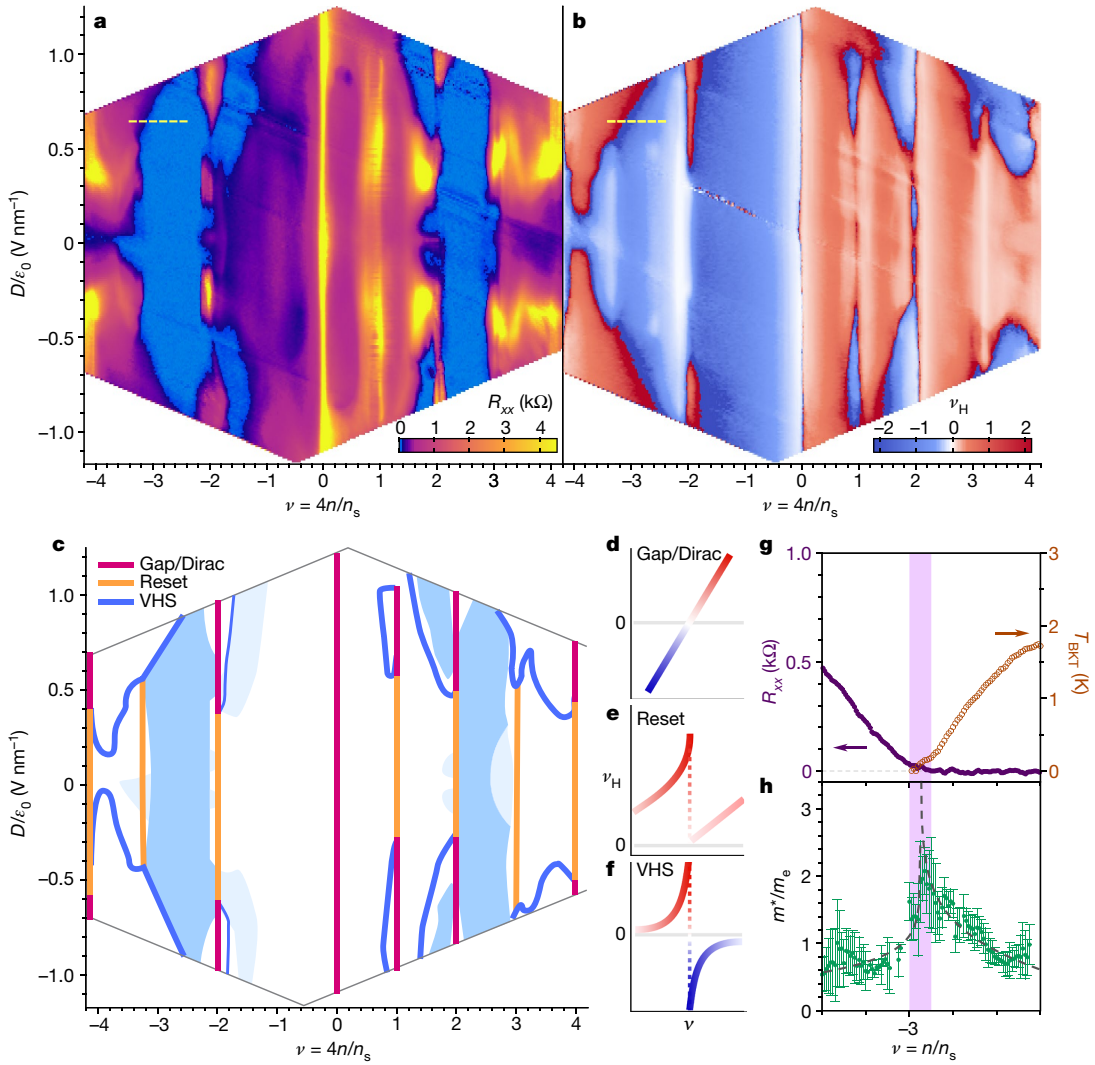

Fig. 2 | MATTG phase diagrams. a, **b**, R_{xx} at $B = 0$ T (**a**) and normalized Hall density $\nu_H = 4n_H/n_s$ at $B = \pm 1.5$ T (**b**), versus ν and D. Data are taken at $T = 70$ mK. Superconductivity is represented by bright blue regions in **a**. **c**, Schematic sketches of the three types of feature found in the Hall density in **b**, and denoted by 'gap/Dirac' (red), 'reset' (yellow), and 'VHS' (dark blue). The blue regions in **c** denote the superconducting phase as determined in **a**. The branches near $\nu = -2 + \delta$ at large D and the regions at small D, all denoted by light blue, correspond to very weak superconductivity. The behaviour of ν_H versus ν for each of these features is shown in **d**–**f**. **d**, At a 'gap/Dirac' feature, ν_H changes linearly with ν while crossing zero. **e**, At a 'reset' feature, ν_H rapidly drops to zero but without changing sign (here shown for $\nu > 0$). **f**, At a 'VHS' feature, ν_H diverges and changes sign at a Van Hove singularity. In **d**–**f**, the colour shading represents the expected colour in **b** across each type of feature. **g**, **h**, Plots of R_{xx} (purple) and the BKT transition temperature T_{BKT} (brown; **g**), and effective mass m^* as function of ν (**h**), taken at the displacement field indicated by the yellow dashed line in **a**, **b**: $D/\varepsilon_0 = 0.64$ V nm^{-1}. T_{BKT} approaches zero and m^* shows a peak around the VHS, which is represented by the pink region. m_e is the electron mass. In **h**, the dashed guidelines correspond to a logarithmic divergence in the DOS at the VHS, and the error bars correspond to a confidence interval of 0.9.

superlattice, $\nu = 4n/n_s = +1, \pm 2, +3, \pm 4$ appear as vertical features, regardless of D, where n is the carrier density and $n_s = 8\theta^2/(\sqrt{3}a^2)$ is the superlattice density ($a = 0.246$ nm is the graphene lattice constant). At zero D, we find an extra set of quantum oscillations that emanates from the charge-neutrality point (Fig. 1d), which vanishes when a moderate D is applied (Fig. 1e). These observations are consistent with a coexisting dispersive band tunable by D, as predicted by calculations (Fig. 1b, c). We further confirm the Dirac character of the dispersive band by measuring its quantum Hall sequence (Fig. 1f). By tracking the Dirac Landau levels, we estimate the chemical potential μ in the flat bands as a function of ν (Methods). We find 'pinning' of the chemical potential near each integer ν (Fig. 1g), indicating a cascade of phase transitions similar to that observed in MATBG[27–29]. We estimate the many-body bandwidth of the flat bands to be around 100 meV (40 meV on the hole side and 60 meV on the electron side), relatively large compared to the approximately 40–60 meV many-body bandwidth in MATBG[27,29].

When MATTG is doped near $\nu = \pm 2$, we find robust superconducting phases. Figure 1h, i shows the superconducting domes in the hole-doped (near $\nu = -2$) and electron-doped (near $\nu = +2$) sides at optimal displacement fields. We find strong superconductivity with a $T_c^{50\%}$ (see Methods section 'T_c and coherence-length analysis') of approximately 2.9 K and approximately 1.4 K for the regions $\nu = -2 - \delta$ and $\nu = +2 + \delta$, respectively ($0 < \delta < 1$), and weaker superconductivity with $T_c^{50\%} < 1$ K for the $\nu = -2 + \delta$ and $\nu = +2 - \delta$ regions. Figure 1j shows the longitudinal voltage–current (V_{xx}–I) characteristics in the $\nu = -2 - \delta$ dome as a function of T, exhibiting clear BKT-transition behaviour, from which we extracted $T_{BKT} \approx 2.1$ K. Alternatively, the Halperin–Nelson fit[30] of the longitudinal resistance R_{xx} versus T (Fig. 1j, top-left inset) gives a consistent value of $T_{BKT} \approx 2.25$ K. The V_{xx}–I curve at the lowest temperature shows a zero resistance plateau up to a critical current $I_c \approx 600$ nA, above which the system switches sharply to a resistive state. The sharp transitions and associated hysteresis (Extended Data Fig. 4) are characteristic of robust

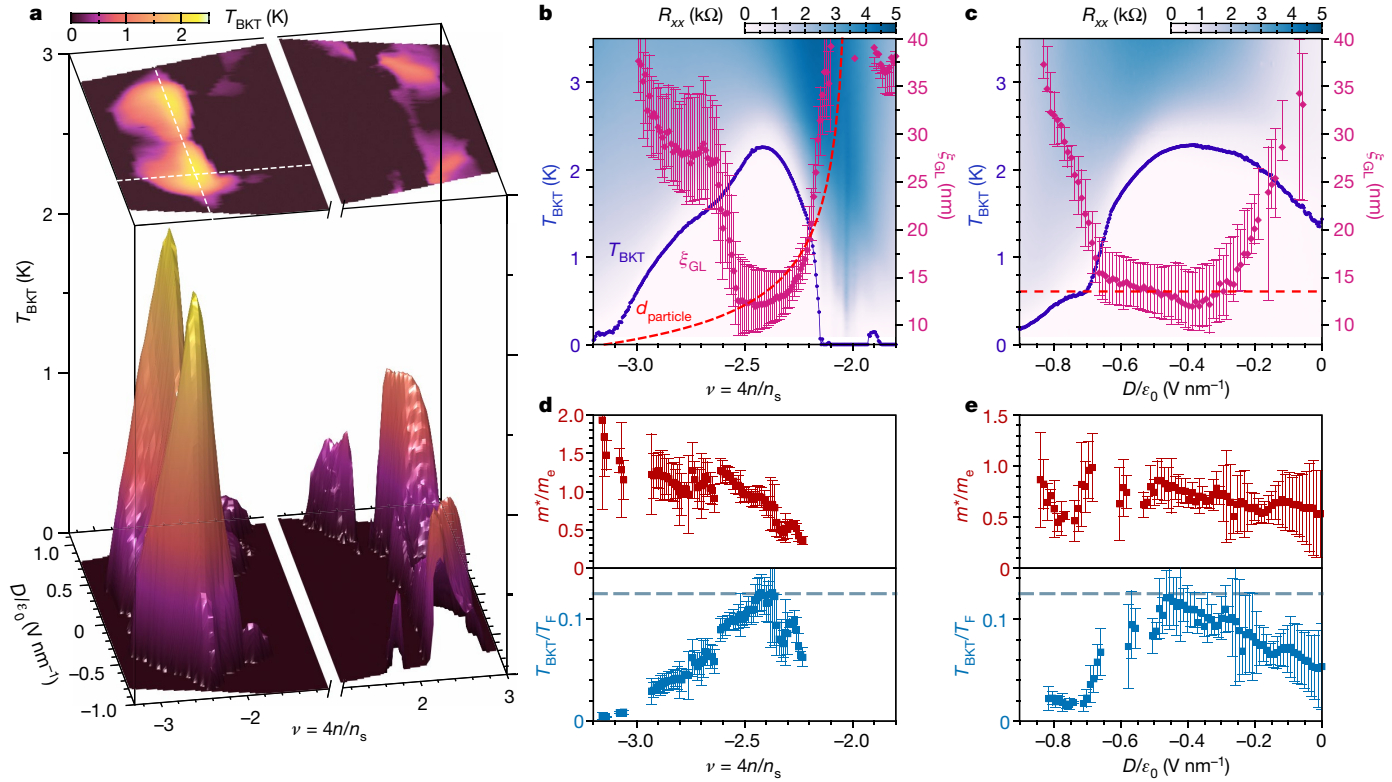

Fig. 3 | Ultrastrong-coupling superconductivity and proximity to the BCS–BEC crossover. a, Three-dimensional map of the BKT transition temperature T_{BKT} versus ν and D. The optimal (ν_{opt}, D_{opt}/ε_0) point corresponding to the maximum T_{BKT} is (−2.4, −0.44 V nm^{-1}). **b**, **c**, Line cuts of T_{BKT} and the extracted Ginzburg–Landau coherence length ξ_{GL} versus ν (**b**), and D (**c**), while the other variable is kept at the optimal value (white dashed lines in **a**). The data points for ξ_{GL} were extracted using $T_c^{40\%}$, and the error bars show the values extracted with $T_c^{30\%}$ (top) and $T_c^{50\%}$ (bottom), respectively (see Methods for details). The red dashed lines show the expected interparticle distance $d_{particle} = |n^*|^{-1/2}$ for the carrier density n^*, which starts counting from $\nu = -2$, $n^* = (|\nu| - 2|)n_s/4$. The Ginzburg–Landau coherence length approaches the interparticle distance around the optimal point in the phase diagram where T_{BKT} is the highest. The background colour plot shows R_{xx} versus T and ν. **d**, **e**, Effective mass m^* in units of m_e (upper panel) and the ratio T_{BKT}/T_F (lower panel) as a function of ν (**d**) and D (**e**; same line cuts as in **b**, **c**). The Fermi temperature is calculated from $T_F = \pi\hbar^2 n^*/(m^* k_B)$. Around optimal doping and displacement field, T_{BKT}/T_F approaches the blue dashed line, which represents the upper bound of T_{BKT}/T_F in the BCS–BEC crossover in two dimensions, the value of which is 0.125. The error bars in **d**, **e** correspond to a confidence interval of 0.9.

superconducting behaviour, which cannot be accounted for by alternative mechanisms, such as Joule heating[31]. To further confirm the superconductivity, we measure the critical current in the $\nu = +2 + \delta$ dome, near its boundary with the resistive feature, as a function of perpendicular magnetic field B. We find a clear Fraunhofer-like oscillation pattern (Fig. 1l), which can be explained by the interference between superconducting percolation paths separated by normal regions due to charge inhomogeneity, and constitutes a direct demonstration of Josephson phase coherence in MATTG. On the other hand, the B-dependence of I_c at optimal doping, near $\nu = -2 - \delta$, does not show a visible oscillatory behaviour, probably owing to the lack of normal islands in this strong superconducting regime (Fig. 1k). Instead, we find a long superconducting 'tail' that remains up to 400 mT, suggesting a high critical magnetic field B_{c2} at this density.

Tunable phase boundaries

MATTG exhibits a rich phase diagram as a function of ν, D, T and B. In particular, the prominent D dependence enables us to correlate the evolution of the superconducting phase boundaries with normal-state magnetotransport features, which can provide important insight into the nature of the superconductivity. Figure 2a shows R_{xx} as a function of ν and D. Various resistive features can be seen, especially at $\nu = +1$, ±2, +3, ±4, some of which have substantial D dependence (Extended Data Fig. 5). In addition, there are zero resistance regions, shown in bright blue, denoting superconductivity. These superconducting regions are most prominent between $|\nu| = 2$ and $|\nu| = 3$, though they can also extend into neighbouring regions. The extended regions at small D could be due to the interplay with the Dirac bands. Figure 2b shows the normalized Hall density $\nu_H = 4n_H/n_s$, where $n_H = -[e(dR_{xy}/dB)]^{-1}$ (e, electron charge) and R_{xy} is the Hall resistance (Extended Data Fig. 6). In MATTG, the Hall density exhibits three main types of behaviour, characterized by a different dependence on ν: 'gap/Dirac', 'reset' and 'VHS' (Van Hove singularity), as illustrated in Fig. 2d–f. The trajectories of these features are summarized in Fig. 2c, along with the phase boundaries of superconductivity. The first type, 'gap/Dirac', denotes a continuous zero crossing of ν_H as ν is increased (Fig. 2d). This behaviour indicates that the Fermi level crosses a gap or Dirac-like point. The second type is a 'reset' to zero, that is, ν_H drops/rises suddenly close to zero but it does not change sign, and it starts rising/dropping again in the same direction as it was before the 'reset' (see Fig. 2e for electron side). It is typically observed across certain integer filling factors in MATBG[3,4], associated with the Coulomb-induced phase transitions[27–29], and also occurs in MATTG near zero and small displacement fields. Both types of features occur only close to integer fillings $\nu = 0, \pm1, \pm2, \ldots$ By contrast, the third type of feature exhibits a divergent ν_H with a zero crossing (Fig. 2f), which is associated with saddle-points on the Fermi surface known as Van Hove singularities. At a VHS, ν_H ceases to represent the number of carriers in the system, as the electrons no longer follow a closed semi-classical orbit. In two dimensions, the density of states (DOS) at a VHS diverges and, in general, there is no restriction on the density at which a VHS occurs.

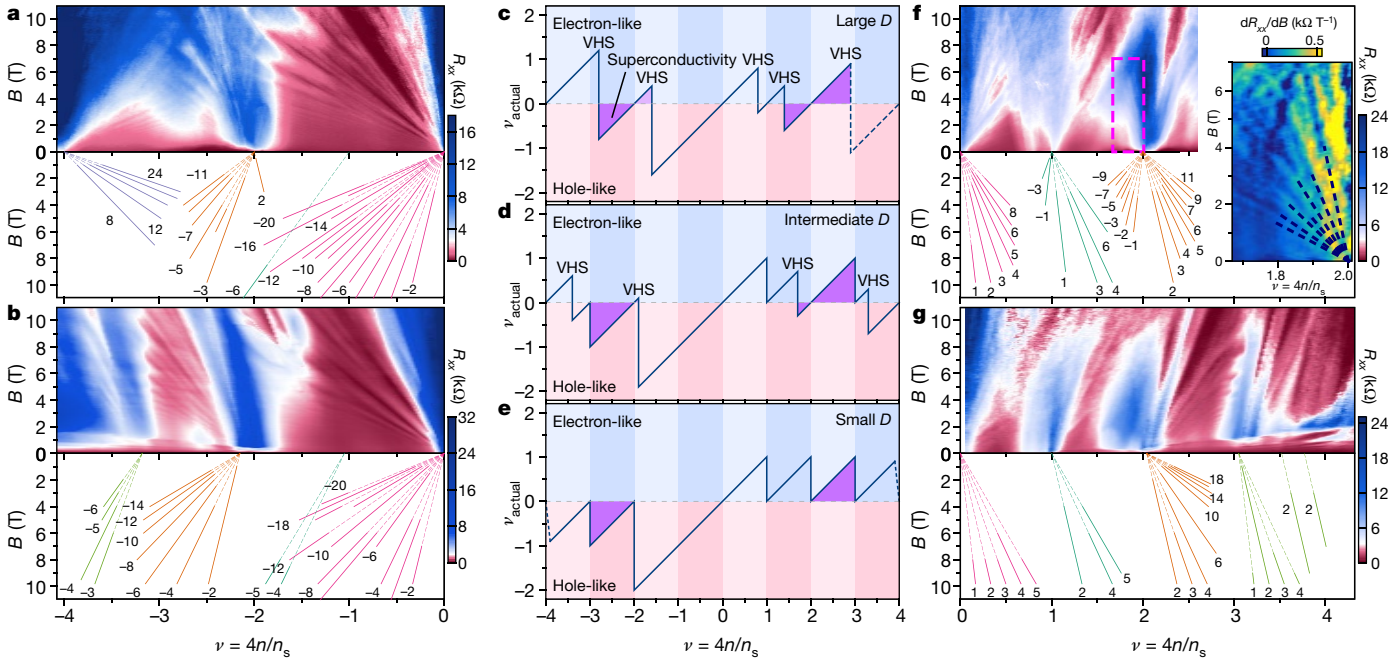

Fig. 4 | Connection between superconductivity and carriers emerging from the $|\nu|=2$ phase. a, **b**, Landau fan diagrams (R_{xx} versus ν and B, upper panel) and their Landau level designations (lower panel) in the hole-doped side ($\nu<0$) for large D ($D/\varepsilon_0=-0.64$ V nm^{-1}), and small D ($D/\varepsilon_0=0$ V nm^{-1}), respectively (see Extended Data Fig. 9 for intermediate D). **c**–**e**, Schematic summaries of the carrier types and numbers corresponding to large, intermediate and small D, respectively, with superconducting regions denoted by purple shades. **f**, **g**, Landau fan diagrams and designations in the electron-doped side ($\nu>0$) at $D/\varepsilon_0=-0.77$ V nm^{-1} (**f**) and $D/\varepsilon_0=0$ V nm^{-1} (**g**; see Extended Data Fig. 9 for an intermediate D). The inset in **f** shows the derivative dR_{xx}/dB of the region denoted by the pink dashed rectangle in the upper panel. These Landau fans indicate that at small D, the carriers are always hole-like (electron-like) on the $-4<\nu<0$ ($0<\nu<4$) side, and 'resets' occur at $\nu=+1, \pm2, \pm3$, similar to previous studies in MATBG. On the other hand, at large D, carriers with opposite polarity (that is, electron-like at $-4<\nu<0$ or hole-like at $0<\nu<4$) dominate near $\nu\gtrsim-4$, -2 ($\nu\lesssim+2$, $+4$). The VHSs are responsible for the transitions between carriers with different polarities. The 'resets' near $|\nu|=3$ are no longer present, and the outward-facing Landau fans from $|\nu|=2$ directly meet the inward-facing fans from $|\nu|=4$ at VHSs. We find that superconductivity is only found in the regions where the carriers originate from the $\nu=\pm2$ states, that is, when the Landau fan at that density converges towards $\nu=\pm2$. The large-ν regions in **c** and **f** are limited by the maximum gate value we can apply before leakage, but the trend of the carrier dynamics can be deduced from the Hall density map in Fig. 2b. (We note that at small D there are slight shifts in ν, which may be attributed to interplay with the Dirac bands.).

We find experimentally that they evolve and can merge with the other two types of features as D is varied.

We find that superconductivity emanating from $\nu=\pm2$ is consistently suppressed upon reaching VHS—that is, the superconductivity is 'bounded' by the VHS contours, as well as at the 'resets' near $\nu=\pm3$. Figure 2g shows R_{xx} versus ν at $D/\varepsilon_0=0.64$ V nm^{-1} (ε_0, vacuum permittivity; yellow dashed line in Fig. 2a), and on the same plot T_{BKT} versus ν. T_{BKT} falls to 0 K, and R_{xx} begins rising, as the VHS around $\nu=-2.9$ (denoted by pink shading) is reached. To further confirm the occurrence of the VHS, we investigate the effective mass m^* versus ν, measured through quantum oscillations, at the same D (Methods and Extended Data Fig. 7). It exhibits a divergent trend near the VHS, as expected in a 2D system. We note that the Hall density signature of the VHS bounding the $\nu=-2+\delta$ superconducting dome appearing at large D, which has a lower T_c than in the $\nu=-2-\delta$ dome, requires a smaller magnetic field of $B\approx0.1$–0.3 T to reveal it (Extended Data Fig. 6).

The observation that superconductivity vanishes right at the VHS is highly unusual. In Bardeen–Cooper–Schrieffer (BCS) superconductors, the order parameter and related quantities (T_c, I_c, and so on) are generally positively correlated with the DOS of the parent state at the Fermi level. This trend is directly seen in the weak-coupling BCS theory formula for $T_c\propto\exp(-1/\lambda N)$ (where N is the DOS at the Fermi level), regardless of whether the coupling λ originates from electron–phonon coupling, spin fluctuations, or other mechanisms. In particular, a divergent DOS at a VHS has been predicted to induce or enhance the superconducting order in various systems[32–34]. Our observation of the opposite trend therefore indicates that the superconductivity in MATTG is unlikely to be consistent with conventional weak-coupling BCS theory. We emphasize that this clear demonstration of a separation between the strength of the superconductivity and the Fermi surface topology is accessible only in MATTG at large D, where a VHS can be tuned near the vicinity of the superconducting region. This does not occur at small D in MATTG, and this tunability is absent in MATBG.

Ultrastrong-coupling superconductivity

The wide tunability of the MATTG system enables us to investigate in detail the coupling strength of the superconducting state by measuring the Ginzburg–Landau coherence length ξ_{GL} as a function of various parameters. We first obtain a map of T_{BKT} in the entire phase space of ν and D to understand the evolution of the superconductivity (Fig. 3a). The zero-temperature superconducting coherence length $\xi_{GL}(0)$ can be determined by measuring the critical temperatures T_c at different perpendicular magnetic fields B (Methods and Extended Data Fig. 8). We perform this analysis as a function of either ν or D, while the other parameter is kept fixed at the optimal point, and the extracted ξ_{GL} values are overlaid on the corresponding T_{BKT} plots in Fig. 3b, c. We find that MATTG has an extremely short coherence length, reaching down to $\xi_{GL}(0)\approx12$ nm near the optimal point, which is comparable to the interparticle distance. For comparison, in Fig. 3b, c we show the expected mean interparticle distance $d_{particle}=|n^*|^{-1/2}$, where $n^*=(|\nu|-2|)n_s/4$ is the carrier density counting from $\nu=-2$ (as suggested by both quantum oscillations and Hall density measurements, see Fig. 4 and Extended Data Fig. 6). In the 'underdoped' region of the

superconducting dome ($-2.4 < \nu < -2.15$), we find that the coherence length is bounded by the interparticle distance.

These observations constitute a first indication that MATTG is a superconductor that can be tuned close to the BCS–BEC (Bose–Einstein condensate) crossover. The saturation of ξ_{GL} at the interparticle distance suggests that a large fraction of the available carriers are condensed into Cooper pairs, that is, $n_{sf}/n^* \lesssim 1$, where n_{sf} is the superfluid density, in contrast to conventional superconductors where only a tiny fraction of electrons are condensed. This difference can be captured in the framework of the BCS–BEC crossover, as the system is tuned from the weak coupling regime ($T_c/T_F \ll 0.1$) to the ultrastrong-coupling regime ($T_c/T_F \gtrsim 0.1$). To estimate how close MATTG near its optimal doping is to the BCS–BEC crossover, we measure the ratio T_{BKT}/T_F as a function of ν and D (Fig. 3d, e). As true long-range order does not exist in two dimensions, in both the BCS and BEC limits the superfluid undergoes a BKT transition at[35] $T_{BKT} \propto n_{sf}/m^*$. We can therefore use the ratio T_{BKT}/T_F to quantify the superfluid fraction n_{sf}/n^* in both regimes. In the BCS–BEC crossover in two dimensions, T_{BKT}/T_F has an upper bound of[36] 0.125. Our experimentally extracted T_{BKT}/T_F reaches values in excess of 0.1, with maximum values close to 0.125. This indicates that the superconductivity in MATTG is probably of strong-coupling nature, and possibly close to the BCS–BEC crossover. For comparison with other strong 2D superconductors, $T_{BKT}/T_F \approx 0.05$ ($T_c/T_F \approx 0.08$) in MATBG[4], and $T_c/T_F \approx 0.04$ in Li_xHfNCl[37]. Another strong 2D superconductor is monolayer FeSe grown on STO, for which very high T_c/T_F values, of the order of approximately 0.1, have been reported[38], though transport data show substantially broad R–T transitions, which may indicate a lower T_{BKT}/T_F value[38].

Superconductivity emerges from the $|\nu| = 2$ phase

To gain further insight into the MATTG superconducting phase diagram, we analyse the type of carriers involved in the superconductivity. Figure 4a, b shows quantum oscillations measurements in the $-4 < \nu < 0$ range, at large and small displacement field, respectively. The corresponding data for electrons—that is, in the $0 < \nu < +4$ range—are shown in Fig. 4f, g. At small D (including zero) there is a 'reset' at $|\nu| = 2$, which manifests as an outward-facing (away from $\nu = 0$) Landau fan originating from $|\nu| = 2$ (Fig. 4b, g). These fans end near $|\nu| = 3$, where new outward fans start, consistent with the 'resets' occurring there (Fig. 2b, c), which indicates phase transitions to a different broken-symmetry-phase ground state[27–29]. At these small D values, the superconductivity is restricted to the regions between $|\nu| = 2$ and $|\nu| = 3$ (Fig. 2a–c), a behaviour summarized in Fig. 4e.

At large D, the phase diagram changes substantially (Fig. 2), where superconductivity is now bounded by VHSs in some regions, and extra superconducting branches appear, particularly strong for $\nu = +2 - \delta$ (Fig. 3a). These features are correlated with inward-facing (towards charge neutrality) fans that start to develop at $|\nu| = 2$ (Fig. 4a, f), which meet the fans from $\nu = 0$ (hole side) or $\nu = +1$ (electron side) at a VHS. This indicates that the states that result from the removal of electrons (holes) from $\nu = +2$ ($\nu = -2$) remain adiabatically connected to the ground state at $|\nu| = 2$, until the VHS is reached. This is different from the small-D case, where the system immediately goes through a phase transition across the 'resets'. The data at intermediate D are shown in Extended Data Fig. 9. The evolution between the 'reset'-type features and 'VHS'-type features might be related to a change in the bandwidth and band topology as the Dirac bands start to hybridize with the flat bands (Fig. 1b, c). As one possibility, it has been suggested that the positions of the VHSs in the single-particle flat bands help determine the occurrence of a flavour-symmetry-breaking phase transition, as well as the filling factor at which they occur[39]. When symmetry breaking occurs right at integer fillings, it appears as a 'reset'; when it occurs slightly before the integer fillings, it appears as a 'VHS' feature in the Hall density at the phase transition, followed by a 'gap/Dirac' feature at the integer filling[39].

For both cases, we find the superconductivity to be still bounded within the regions where the carriers are connected to the $|\nu| = 2$ ground state, as summarized in Fig. 4c, d. These observations indicate that the many-body ground state emerging from the broken-symmetry phase transition at $|\nu| = 2$ has an essential role in forming robust superconductivity, since superconductivity appears as carriers are added to or subtracted from that state, and it vanishes when the normal state of the system changes to a different phase, either through a 'reset' to the $|\nu| = 3$ broken-symmetry phase (at small D) or through a VHS to $\nu = 0$, $\nu = +1$, or $|\nu| = 4$ phases at large D.

Our experiments point towards a strong coupling mechanism for superconductivity that is deeply tied to the ground state at $\nu = \pm 2$, and where the maximum T_c is mostly determined by the carrier density instead of the precise structure of the DOS. At the same time, we also note that the presence of a VHS can affect the phase transitions that underlie the broken-symmetry phases. These observations should be taken into consideration in the development of theoretical models for moiré superconductors with ultrastrong coupling strength. It is noteworthy to determine what it is that makes MATBG and MATTG robust superconductors. One possibility is that they both have certain symmetry properties, in particular approximate C_2 symmetry[40]. Interestingly, this symmetry is absent in other graphene-based moiré systems. We hope future investigations on other C_2-symmetric moiré systems will determine if this symmetry is indispensable for the formation of strong-coupling superconductivity in moiré flat bands.

Online content

Any methods, additional references, Nature Research reporting summaries, source data, extended data, supplementary information, acknowledgements, peer review information; details of author contributions and competing interests; and statements of data and code availability are available at https://doi.org/10.1038/s41586-021-03192-0.

1. Suárez Morell, E., Correa, J. D., Vargas, P., Pacheco, M. & Barticevic, Z. Flat bands in slightly twisted bilayer graphene: tight-binding calculations. *Phys. Rev. B* **82**, 121407 (2010).
2. Bistritzer, R. & MacDonald, A. H. Moiré bands in twisted double-layer graphene. *Proc. Natl Acad. Sci. USA* **108**, 12233–12237 (2011).
3. Cao, Y. et al. Correlated insulator behaviour at half-filling in magic-angle graphene superlattices. *Nature* **556**, 80–84 (2018).
4. Cao, Y. et al. Unconventional superconductivity in magic-angle graphene superlattices. *Nature* **556**, 43–50 (2018).
5. Yankowitz, M. et al. Tuning superconductivity in twisted bilayer graphene. *Science* **363**, 1059–1064 (2019).
6. Lu, X. et al. Superconductors, orbital magnets and correlated states in magic-angle bilayer graphene. *Nature* **574**, 653–657 (2019).
7. Chen, G. et al. Evidence of a gate-tunable Mott insulator in a trilayer graphene moiré superlattice. *Nat. Phys.* **15**, 237–241 (2019).
8. Burg, G. W. et al. Correlated insulating states in twisted double bilayer graphene. *Phys. Rev. Lett.* **123**, 197702 (2019).
9. Shen, C. et al. Correlated states in twisted double bilayer graphene. *Nat. Phys.* **16**, 520–525 (2020).
10. Cao, Y. et al. Tunable correlated states and spin-polarized phases in twisted bilayer–bilayer graphene. *Nature* **583**, 215–220 (2020).
11. Liu, X. et al. Tunable spin-polarized correlated states in twisted double bilayer graphene. *Nature* **583**, 221–225 (2020).
12. Polshyn, H. et al. Electrical switching of magnetic order in an orbital Chern insulator. *Nature* **588**, 66–70 (2020).
13. Shi, Y. et al. Tunable Van Hove singularities and correlated states in twisted trilayer graphene. Preprint at https://arxiv.org/abs/2004.12414 (2020).
14. Chen, S. et al. Electrically tunable correlated and topological states in twisted monolayer–bilayer graphene. *Nat. Phys.* https://doi.org/10.1038/s41567-020-01062-6 (2020).
15. Regan, E. C. et al. Mott and generalized Wigner crystal states in WSe_2/WS_2 moiré superlattices. *Nature* **579**, 359–363 (2020).
16. Tang, Y. et al. Simulation of Hubbard model physics in WSe_2/WS_2 moiré superlattices. *Nature* **579**, 353–358 (2020).
17. Wang, L. et al. Correlated electronic phases in twisted bilayer transition metal dichalcogenides. *Nat. Mater.* **19**, 861–866 (2020).
18. Khalaf, E., Kruchkov, A. J., Tarnopolsky, G. & Vishwanath, A. Magic angle hierarchy in twisted graphene multilayers. *Phys. Rev. B* **100**, 085109 (2019).
19. Sharpe, A. L. et al. Emergent ferromagnetism near three-quarters filling in twisted bilayer graphene. *Science* **365**, 605–608 (2019).
20. Serlin, M. et al. Intrinsic quantized anomalous Hall effect in a moiré heterostructure. *Science* **367**, 900–903 (2020).

21. Chen, G. et al. Tunable correlated Chern insulator and ferromagnetism in a moiré superlattice. *Nature* **579**, 56–61 (2020); correction **581**, E3 (2020).
22. Chen, G. et al. Signatures of tunable superconductivity in a trilayer graphene moiré superlattice. *Nature* **572**, 215–219 (2019).
23. Tsai, K.-T. et al. Correlated insulating states and transport signature of superconductivity in twisted trilayer graphene moiré of moiré superlattices. Preprint at https://arxiv.org/abs/1912.03375 (2019).
24. Mora, C., Regnault, N. & Bernevig, B. A. Flatbands and perfect metal in trilayer moiré graphene. *Phys. Rev. Lett.* **123**, 026402 (2019).
25. Carr, S. et al. Ultraheavy and ultrarelativistic Dirac quasiparticles in sandwiched graphenes. *Nano Lett.* **20**, 3030–3038 (2020).
26. Lei, C., Linhart, L., Qin, W., Libisch, F. & MacDonald, A. H. Mirror-symmetry breaking and stacking-shift dependence in twisted trilayer graphene. Preprint at https://arxiv.org/abs/2010.05787 (2020).
27. Park, J. M., Cao, Y., Watanabe, K., Taniguchi, T. & Jarillo-Herrero, P. Flavour Hund's coupling, correlated Chern gaps, and diffusivity in moiré flat bands. Preprint at https://arxiv.org/abs/2008.12296 (2020).
28. Wong, D. et al. Cascade of electronic transitions in magic-angle twisted bilayer graphene. *Nature* **582**, 198–202 (2020).
29. Zondiner, U. et al. Cascade of phase transitions and Dirac revivals in magic-angle graphene. *Nature* **582**, 203–208 (2020).
30. Halperin, B. I. & Nelson, D. R. Resistive transition in superconducting films. *J. Low Temp. Phys.* **36**, 599–616 (1979).
31. He, M. et al. Symmetry breaking in twisted double bilayer graphene. *Nat. Phys.* **17**, 26–30, (2021).
32. Nandkishore, R., Levitov, L. S. & Chubukov, A. V. Chiral superconductivity from repulsive interactions in doped graphene. *Nat. Phys.* **8**, 158–163 (2012).
33. Dessau, D. S. et al. Key features in the measured band structure of $Bi_2Sr_2CaCu_2O_{8+\delta}$: flat bands at E_F and Fermi surface nesting. *Phys. Rev. Lett.* **71**, 2781–2784 (1993).
34. Yokoya, T. et al. Extended Van Hove singularity in a noncuprate layered superconductor Sr_2RuO_4. *Phys. Rev. Lett.* **76**, 3009–3012 (1996).
35. Nelson, D. R. & Kosterlitz, J. M. Universal jump in the superfluid density of two-dimensional superfluids. *Phys. Rev. Lett.* **39**, 1201–1205 (1977).
36. Hazra, T., Verma, N. & Randeria, M. Bounds on the superconducting transition temperature: applications to twisted bilayer graphene and cold atoms. *Phys. Rev. X* **9**, 031049 (2019).
37. Nakagawa, Y. et al. Gate-controlled low carrier density superconductors: toward the two-dimensional BCS–BEC crossover. *Phys. Rev. B* **98**, 064512 (2018).
38. Wang, Z., Liu, C., Liu, Y. & Wang, J. High-temperature superconductivity in one-unit-cell FeSe films. *J. Phys. Condens. Matter* **29**, 153001 (2017).
39. Xie, M. & MacDonald, A. H. Weak-field Hall resistivity and spin/valley flavor symmetry breaking in MAtBG. Preprint at https://arxiv.org/abs/2010.07928 (2020).
40. Khalaf, E., Chatterjee, S., Bultinck, N., Zaletel, M. P. & Vishwanath, A. Charged skyrmions and topological origin of superconductivity in magic-angle graphene. Preprint at https://arxiv.org/abs/2004.00638 (2020).

Methods

Sample fabrication

Our samples consist of three sheets of monolayer graphene, with twist angles θ and $-\theta$ for the top/middle and middle/bottom interfaces, respectively, which are then sandwiched between two hexagonal boron nitride (hBN) flakes approximately 30–80 nm thick. We first exfoliate the hBN and graphene flakes on SiO_2/Si substrates, and analyse these flakes with optical microscopy. The multilayer stack is fabricated using a dry pick-up technique, where a layer of poly(bisphenol A carbonate)/polydimethylsiloxane (PC/PDMS) on a glass slide is used to pick up the flakes sequentially using a micro-positioning stage. To ensure the angle alignment between the graphene layers and to reduce strain, they are cut in situ from a single monolayer graphene flake using a focused laser beam[27]. The hBN flakes are picked up while heating the stage to 90 °C, while the graphene layers are picked up at room temperature. The resulting structure is released on the prepared hBN on Pd/Au stack at 175 °C. We define the Hall bar geometry with electron-beam lithography and reactive ion etching. The top gate and electrical contacts are thermally evaporated using Cr/Au. Schematics and optical picture of the finished devices are shown in Extended Data Fig. 2.

Measurement setup

Transport data are measured in a dilution refrigerator with a base electronic temperature of ~70 mK. Current through the sample and the four-probe voltage are first amplified by 10^7 V A^{-1} and 1,000 V A^{-1}, respectively, using current and voltage pre-amplifiers, and then measured with lock-in amplifiers (SR-830), synchronized at the same frequency between approximately 1 and 20 Hz. Current excitation of 1 nA or voltage excitation of 50 μV to 100 μV is used for resistance measurements. For d.c. bias measurements, we use a home-built digital–analogue converter (BabyDAC) passing through a 10-MΩ resistor to provide the d.c. bias current, and measure the d.c. voltage using a digital multimeter (Keysight 34461A) connected to the voltage pre-amplifier.

Bandstructure calculation

The bandstructures shown in Fig. 1b, c are calculated using the continuum model for twisted bilayer graphene[2,41], extended with a third layer on the top that has the same twist angle as the bottommost layer[18,25,26,42]. For simplicity, we neglect the direct coupling from topmost and bottommost layers, and we use off-diagonal and diagonal interlayer hopping parameters $w = 0.1$ eV and $w' = 0.08$ eV, respectively, the latter value empirically accounting for a small relaxation of the lattice. We note that the Fermi velocity of the gapless Dirac bands using these parameters is the same as the value for monolayer graphene.

The colour of the curves in Fig. 1b, c represents the mirror symmetry character of the eigenstates, which we evaluate by projecting the wavefunction of the eigenstate in the topmost layer onto the bottommost layer and calculating its inner product with the wavefunction in the bottommost layer. This evaluates to 1 for a mirror symmetric eigenstate (coloured as orange) and −1 for a mirror antisymmetric eigenstate (coloured as purple), and between −1 and 1 for a nonsymmetric state. We find that at zero displacement field, the flat bands have symmetry character of 1 and the Dirac bands have −1. In other words, the flat bands in MATTG arise from mirror symmetric hopping from the outer layers onto the centre layer. Without a displacement field, the Dirac bands cannot couple to the flat bands, owing to this symmetry protection, though the electrons in the Dirac bands may still participate in the correlation-driven phenomena in the flat bands via Coulomb interactions.

The effect of displacement field is taken into account by imposing an interlayer potential difference $\Delta V = dD/\varepsilon_0$, where $d \approx 0.3$ nm is the interlayer distance. Owing to the screening by the outer layers, the actual electric field between the layers will be less than the externally applied field. Although we can qualitatively capture the effect of the external displacement field in this calculation, a self-consistent treatment is required to accurately solve such a problem, which is beyond the scope of this mostly experimental paper. We note that these calculations do not take into account high-order and non-local interlayer coupling terms, which create a more pronounced particle–hole asymmetry than shown here[25,26,39,42,43].

Stacking alignment

Twisted trilayer graphene has an extra translation degree of freedom compared to twisted bilayer graphene. Although the topmost and bottommost layers are not twisted with respect to each other, their relative stacking order can have a notable effect on the single-particle bandstructure. Among the configurations, the ones with A-tw-A stacking and A-tw-B stacking ('tw' denotes the middle twisted layer) have the highest symmetry, as shown in Extended Data Fig. 1a, b. In particular, only A-tw-A stacking possesses a mirror symmetry; it was shown to have the lowest configuration energy among all possible stacking orders for a given twist angle[25]. Extended Data Fig. 1c–f shows the calculated bandstructures of the A-tw-A and A-tw-B configurations at zero and finite displacement fields. Furthermore, Extended Data Fig. 1g–j shows the calculated Landau level spectrum of the corresponding cases near charge neutrality[44]. In these calculations, we also included a small C_3-symmetry-breaking term[45] to reproduce the fourfold Landau level degeneracy observed in experiments ($\beta = -0.01$, following the convention of a previous work)[45]. We find that in the case of A-tw-A stacking, the Landau level sequence near charge neutrality is ±2, ±6, ±10, …, regardless of whether a displacement field is applied, whereas in the case of A-tw-B stacking, the application of a displacement field leads to a complicated evolution of the Landau level that no longer follows the same sequence. The displacement field also induces a global bandgap in the A-tw-B configuration, while keeping A-tw-A gapless.

From our experimental observations, our MATTG samples are more likely to possess A-tw-A stacking than other configurations, for the following reasons. First, unlike in MATBG, we do not find an insulating state at $\nu = \pm 4$ at any displacement field, suggesting that the system does not have a global energy gap. Second, as shown in Extended Data Fig. 1k, l, the strongest Landau level sequence near the charge neutrality point is always ±2, ±6, ±10, ±14, …, with or without displacement fields. Both of these findings are in agreement with the A-tw-A stacking case, as discussed above. We note that although it is difficult to achieve exactly identical top and bottom angles, from our experiments it seems that a minor difference might not qualitatively affect the role of mirror symmetry.

Chemical-potential estimate

The coexisting flat bands and Dirac bands share the same chemical potential, and so we can use the transport features of the Dirac bands as shown in Fig. 1d to determine the n–μ relationship in the flat bands. Specifically, at a finite magnetic field B and in the absence of D, we assume that the flat bands host a charge density n_f and the Dirac bands host a charge density n_d such that $n = n_f + n_d$.

Under finite B, the Dirac bands are quantized into fourfold degenerate Landau levels labelled by an index $N = 0, \pm 1, \pm 2, \ldots$. In the transport data, if we designate the centres of the R_{xx} peaks (see for example, Fig. 1f) as the centre of the Nth Landau level (not the Landau level gaps), n_d and μ_d follow

$$n_d = \frac{4NB}{\phi_0}, \qquad \mu_d = v_F\sqrt{2e\hbar NB}\,\mathrm{sgn}(N), \tag{1}$$

where $\phi_0 = h/e$ is the flux quantum, the factor 4 accounts for spin and valley degeneracies, and sgn(N) is the sign of N. We use a Fermi velocity of $v_F = 10^6$ m s^{-1} for this estimation. Since n_d and μ_d are functions of

NB only, they are known once we determine the Landau level index *N*, which is evident from the Hall conductivity in the gaps between them, $\sigma_{xy} = 4(N \pm 1/2)e^2/h$ (see Fig. 1f). Therefore, along the trajectory of the *N*th Landau level in an *n*–*B* map, we can determine the n_f–μ_f relationship for the flat bands as

$$n_f = n - \frac{4NB}{\phi_0}, \qquad \mu_f = v_F\sqrt{2e\hbar NB}\,\mathrm{sgn}(N). \tag{2}$$

We performed this extraction for $|N| = 1, 2, 3, 4$ and the results are consistent, as shown in Fig. 1f. The estimated many-body bandwidth of the flat bands from this extraction is around 100 meV, whereas that of MATBG is approximately 40–60 meV (refs. [27,29,46]). This many-body bandwidth includes the Coulomb interaction, which is, in principle, larger in MATTG than in MATBG, owing to the smaller unit cell.

Hall density analysis

The Hall density in Fig. 2b is calculated from R_{xy} measured and anti-symmetrized at $B = 1.5$ T. The reason for choosing this magnetic field is to fully suppress the superconductivity at $\nu = -2 - \delta$, which has a critical magnetic field approaching 1 T, because of the short Ginzburg–Landau coherence length. Extended Data Fig. 6a–c shows representative linecuts in the maps of R_{xx}, R_{xy} and the Hall density ν_H, with the Hall features ('gap/Dirac', 'reset' or 'VHS') and superconducting regions annotated. All major superconducting domes are bounded by the Hall features, although we notice a few exceptions of weak superconductivity that are not bounded. For example, at zero displacement field (Extended Data Fig. 6c), there is a weak signature of superconductivity beyond the reset around $\nu = -3.2$, which has a small but non-zero resistance. We also note that in Fig. 2b, there are some small regions, right before $\nu = +1$ and $\nu = +2$ in some ranges of *D*, where there are signatures of a more complex behaviour in ν_H, with VHSs possibly very close to the 'resets'. These regions need further investigation for a complete understanding.

The weak superconducting region at $\nu = -2 + \delta$ at large *D* is also seemingly not bounded by a VHS in the main Hall density plot taken at $B = \pm 1.5$ T (see Fig. 2a, b). However, we find that signatures of a VHS boundary can be identified if we measure the Hall density using a smaller *B*, as shown in Extended Data Fig. 6d. By comparing to R_{xx} data shown in Extended Data Fig. 6e, we can see that although not perfectly matching, there is a clear correlation between the VHS and the superconductivity boundary. Furthermore, the Landau fans at finite *D* (Fig. 4a, Extended Data Fig. 9a) show signatures of an inward-facing fan at $\nu = -2 + \delta$, supporting the existence of carriers from $\nu = -2$. However, the inward fan, as well as the superconductivity in this region, appears to be extremely fragile, which might be related to why the VHS boundary is invisible when measured at higher *B*.

T_c and coherence-length analysis

The mean-field T_c is extracted by first fitting the high-temperature part of the data to a straight line $r(T) = AT + B$, and then finding the intersection of $R_{xx}(T)$ with $pr(T)$, where *p* is the percentage of normal resistance (we use 50% unless otherwise specified).

We extract the Ginzburg–Landau coherence length from the *B*-dependence of T_c, using the Ginzburg–Landau relation $T_c/T_{c0} = 1 - (2\pi\xi_{GL}^2/\Phi_0)B_\perp$, where $\Phi_0 = h/(2e)$ is the superconducting flux quantum and T_{c0} is the mean-field critical temperature at zero magnetic field (slightly higher than T_{BKT}). As shown in Extended Data Fig. 8, the mean-field T_c at different *B* is extracted at different percentages $p = 30\%$, 40% and 50% of the normal resistance fit (shown as dashed lines). The insets show the extracted T_c using different thresholds. The Ginzburg–Landau coherence length ξ_{GL} is then obtained from a linear fit of T_c versus *B*, the *x* intercept of which is equal to $\Phi_0/(2\pi\xi_{GL}^2)$. The different thresholds yield slightly different but consistent coherence lengths, which we plot as the data points (40%) and error bars (50%, 30%) in Fig. 3b, c. Note that in the presence of charge and/or twist angle disorder, values for ξ_{GL}, T_c and T_{BKT} should be interpreted as spatial averages of the corresponding local quantities.

Effective mass analysis

The effective mass of MATTG is extracted from the *T*-dependent quantum oscillations in a perpendicular magnetic field using the standard Lifshitz–Kosevich formula[47]. Extended Data Fig. 7a, b shows representative quantum oscillations at $\nu = -2.86$ and $\nu = -2.5$, respectively, at $D/\varepsilon_0 = -0.44$ V nm^{-1}. Starting from raw resistance data R_{xx}, we first remove a smooth polynomial background in B^{-1} and obtain ΔR. We then select the most prominent peak/valley in ΔR, and evaluate its change from the valley to the peak as a function of temperature, $\delta R(T)$. We notice that in some curves, such as those shown in Extended Data Fig. 7a, b, the high-field part of the oscillation is either split (Extended Data Fig. 7a) or has a higher periodicity (Extended Data Fig. 7b) than the fundamental frequency that corresponds to the carrier density, which we attribute to broken-symmetry states. We avoid using those peaks for extracting effective mass, as they tend to overestimate the effective mass m^* and underestimate T_F. $\delta R(T)$ is subsequently fitted with the Lifshitz–Kosevich formula

$$\delta R(T) = b\frac{aT}{\sinh(aT)}, \tag{3}$$

where *a* and *b* are fitting parameters. The effective mass m^* is then extracted from

$$m^* = \frac{\hbar e\overline{B}}{2\pi^2 k_B}a, \tag{4}$$

where $\overline{B}$ is the average of the peak and valley positions. The fit is shown in the insets of Extended Data Fig. 7a, b, from which we obtain $m^*/m_e = 1.25 \pm 0.13$ and $m^*/m_e = 0.95 \pm 0.03$, respectively. T_{BKT} at these two points is 1.11 K and 2.09 K, respectively, and so the ratio T_{BKT}/T_F is 0.041 ± 0.004 and 0.100 ± 0.003, respectively.

For the effective-mass data in Fig. 2h and Fig. 3d, e, we performed the extraction with fewer points in temperature, as exemplified in Extended Data Fig. 7c–e. We manually select the peak/valley position (shown as triangles) for each density/displacement field, and the mass is obtained from the same fit as above, as shown in Extended Data Fig. 7f. We have checked that this extraction is consistent with the extraction using more data points in *T* for the representative curves shown (Extended Data Fig. 7a, b), which justifies the analysis with coarser data in *T*.

Data availability

The data that support the current study are available from the corresponding authors upon reasonable and well motivated request.

41. Lopes dos Santos, J. M. B., Peres, N. M. R. & Castro Neto, A. H. Continuum model of the twisted graphene bilayer. *Phys. Rev. B* **86**, 155449 (2012).
42. Lopez-Bezanilla, A. & Lado, J. L. Electrical band flattening, valley flux, and superconductivity in twisted trilayer graphene. *Phys. Rev. Res.* **2**, 033357 (2020).
43. Carr, S., Fang, S., Zhu, Z. & Kaxiras, E. An exact continuum model for low-energy electronic states of twisted bilayer graphene. *Phys. Rev. Res.* **1**, 013001 (2019).
44. Bistritzer, R. & MacDonald, A. H. Moiré butterflies in twisted bilayer graphene. *Phys. Rev. B* **84**, 035440 (2011).
45. Zhang, Y.-H., Po, H. C. & Senthil, T. Landau level degeneracy in twisted bilayer graphene: role of symmetry breaking. *Phys. Rev. B* **100**, 125104 (2019).
46. Tomarken, S. L. et al. Electronic compressibility of magic-angle graphene superlattices. *Phys. Rev. Lett.* **123**, 046601 (2019).
47. Shoenberg, D. *Magnetic Oscillations in Metals* (Cambridge Univ. Press, 1984).
48. Giamarchi, T. & Bhattacharya, S. in *High Magnetic Fields: Applications in Condensed Matter Physics and Spectroscopy* (eds Berthier, C. et al.) 314–360 (2001).

Acknowledgements We thank S. Todadri, A. Vishwanath, S. Kivelson, M. Randeria, S. Ilani, L. Fu and A. Georges for discussions. This work has been primarily supported by the US Department of Energy (DOE), Office of Basic Energy Sciences (BES), Division of Materials Sciences and Engineering under award DE-SC0001819 (J.M.P.). Help with transport measurements and data analysis were supported by the National Science Foundation (DMR-1809802), and the STC Center for Integrated Quantum Materials (NSF grant number DMR-1231319; Y.C.). P.J.-H. acknowledges support from the Gordon and Betty Moore Foundation's EPiQS Initiative through grant GBMF9643. P.J.-H. acknowledges partial support by the Fundación Ramon Areces. The development of new nanofabrication and characterization techniques enabling this work has been supported by the US DOE Office of Science, BES, under award DE-SC0019300. K.W. and T.T. acknowledge support from the Elemental Strategy Initiative conducted by the MEXT, Japan, grant number JPMXP0112101001, JSPS KAKENHI grant numbers JP20H00354 and the CREST (JPMJCR15F3), JST. This work made use of the Materials Research Science and Engineering Center Shared Experimental Facilities supported by the National Science Foundation (DMR-0819762) and of Harvard's Center for Nanoscale Systems, supported by the NSF (ECS-0335765).

Author contributions J.M.P. and Y.C. fabricated the samples, and performed transport measurements and numerical simulations. K.W. and T.T. provided hBN samples. J.M.P., Y.C., and P.J-H. performed data analysis, discussed the results, and wrote the manuscript with input from all co-authors.

Competing interests The authors declare no competing interests.

Additional information

Correspondence and requests for materials should be addressed to Y.C. or P.J.-H.

Peer review information *Nature* thanks Mathias Scheurer, Ke Wang and Guangyu Zhang for their contribution to the peer review of this work.

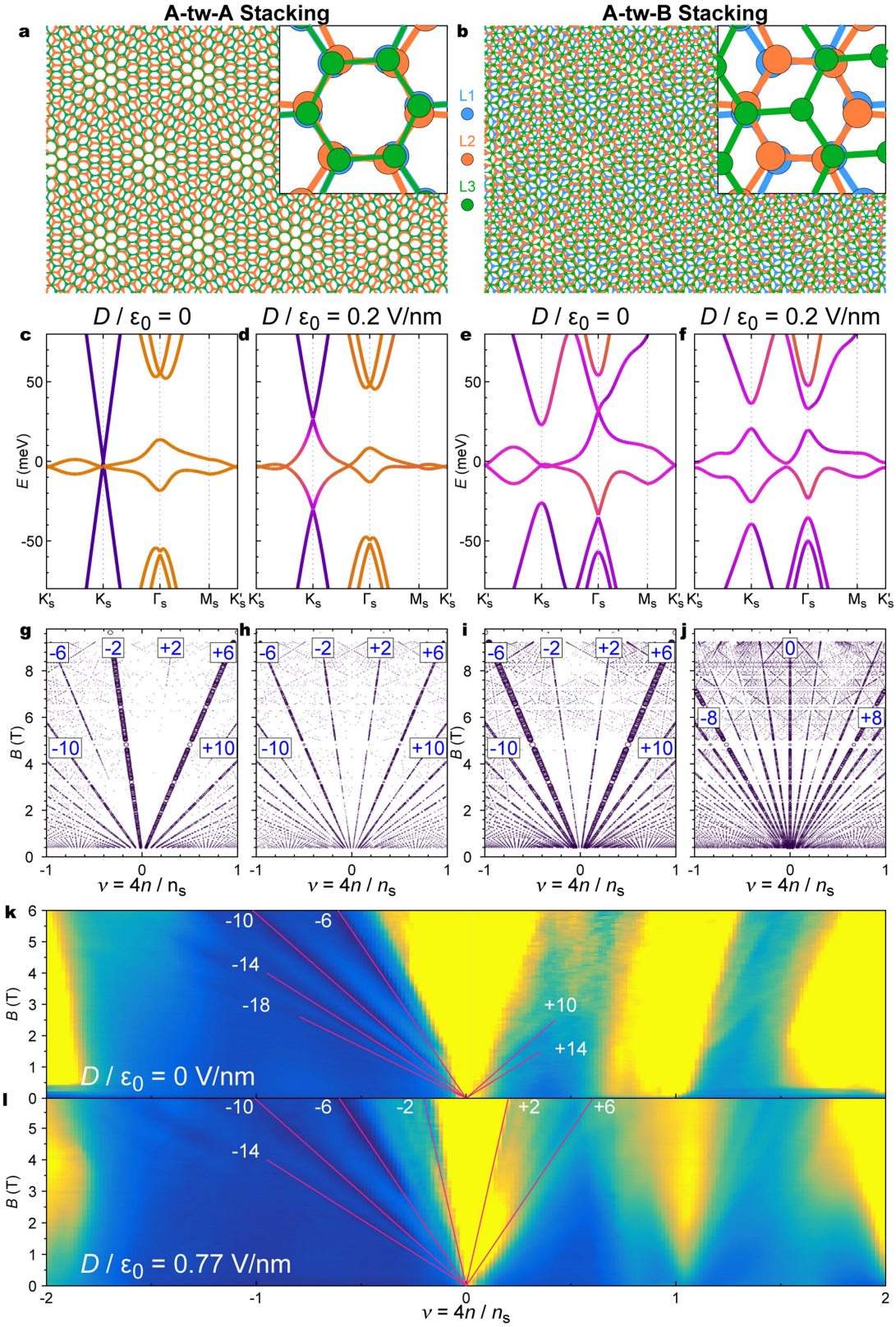

Extended Data Fig. 1 | Stacking order in MATTG. a, **b**, Illustrations of A-tw-A stacking (**a**) and A-tw-B stacking (**b**), where 'tw' denotes the middle twisted layer (L2, orange) and A/B represents the relative stacking order between the topmost (L3, green) and bottommost (L1, blue) layers. **c**–**f**, Continuum-model bandstructures of A-tw-A stacked (**c**, **d**) and A-tw-B stacked (**e**, **f**) MATTG at zero (**c**, **e**) and finite (**d**, **f**) displacement fields. The twist angle is $\theta = 1.57°$ for all plots. **g**–**j**, Calculated Landau level sequence corresponding to the bands in **c**–**f**. The size of the dots represents the size of the Landau level gaps in the Hofstadter spectrum. For A-tw-A stacking, the major sequence of filling factors near the charge neutrality is ±2, ±6, ±10, ..., regardless of the displacement field, whereas for A-tw-B stacking the Landau levels evolve into a symmetry-broken sequence that has 0, ±8 as the dominant filling factors with largest gaps in a finite displacement field. An anisotropy term of $\beta = -0.01$ is included in all of the above calculations (see Methods). **k**, **l**, Experimentally measured Landau levels in MATTG near the charge neutrality. We find the strongest sequence of ±2, ±6, ±10, ... at both $D = 0$ and $D/\varepsilon_0 = 0.77$ V nm^{-1}, consistent with the A-tw-A stacking scenario.

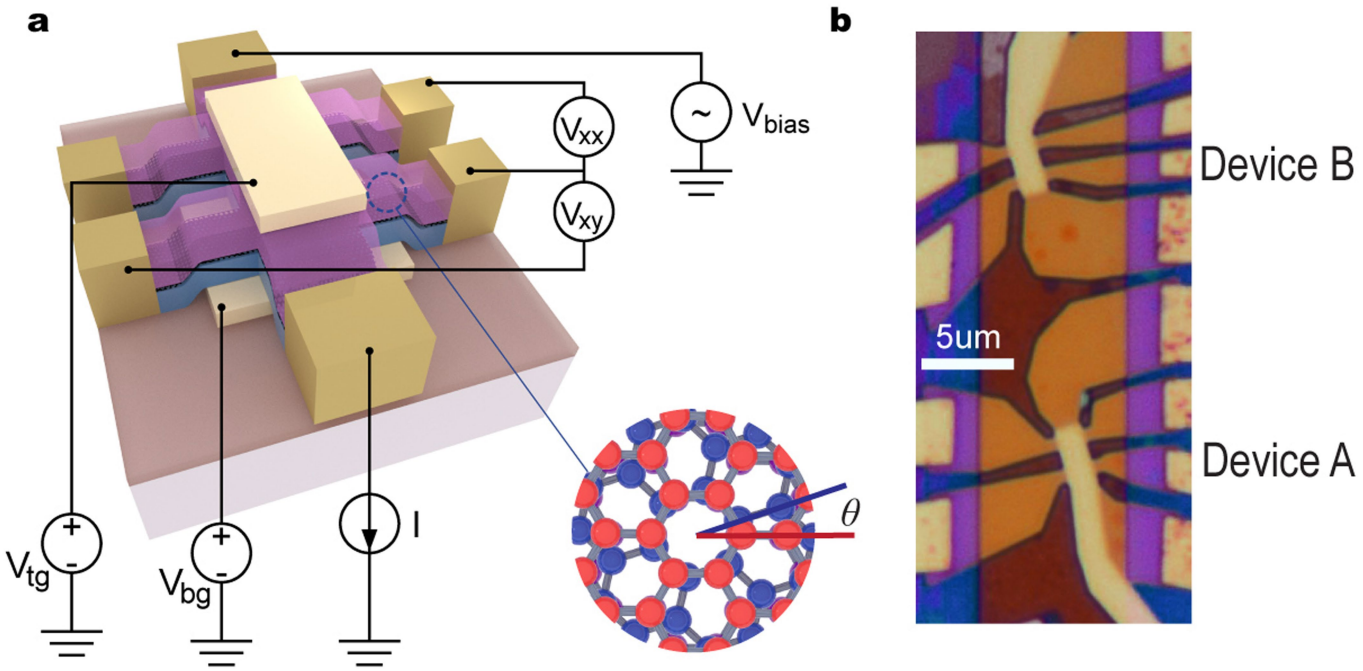

Extended Data Fig. 2 | Device schematics and device optical picture. a, Our device consists of hBN-encapsulated MATTG etched into a Hall bar, Cr/Au contacts on the edge, and top/bottom metallic gates. For transport measurements, we measure current I, longitudinal voltage V_{xx}, and transverse voltage V_{xy}, while tuning the density v and displacement field D by applying top gate voltage V_{tg} and bottom gate voltage V_{bg}. **b**, Optical picture of devices A and B. Device C is lithographically similar.

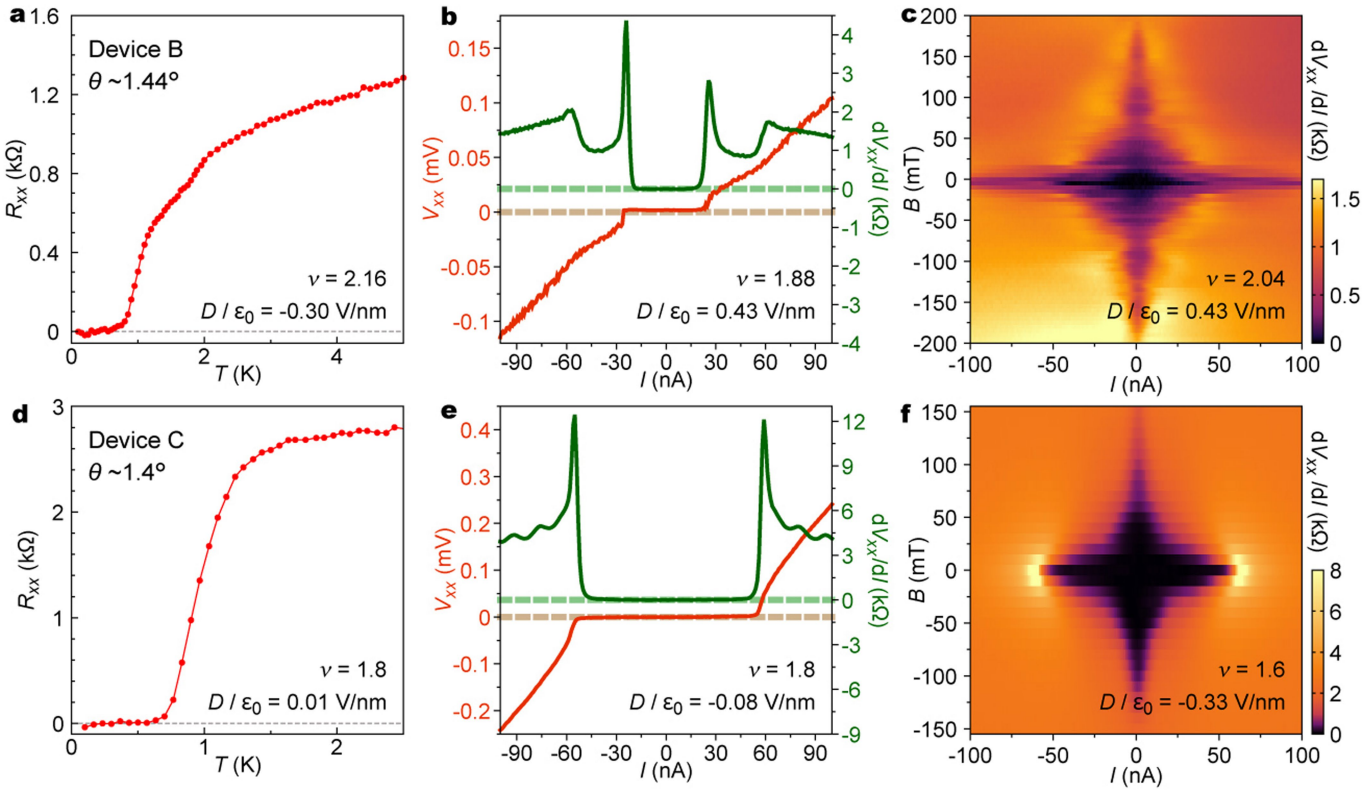

Extended Data Fig. 3 | Robust superconductivity in other MATTG devices (devices B and C). a, R_{xx}–T curve. **b**, V_{xx}–I and dV_{xx}/dI–I curves. **c**, I–B map in device B with a smaller-than-magic-angle $\theta \approx 1.44°$. In this device, maximum $T_{BKT} \approx 0.73$ K. The choice of ν is to display the Fraunhofer-like Josephson interference, which demonstrates the superconducting phase coherence. **d**–**f**, As in **a**–**c**, for device C, with a twist angle $\theta \approx 1.4°$. Device C has a maximum T_{BKT} of ~0.68 K. **f** shows a regular B-suppression of I_c with B. Both devices show sharp peaks in dV_{xx}/dI at their critical currents.

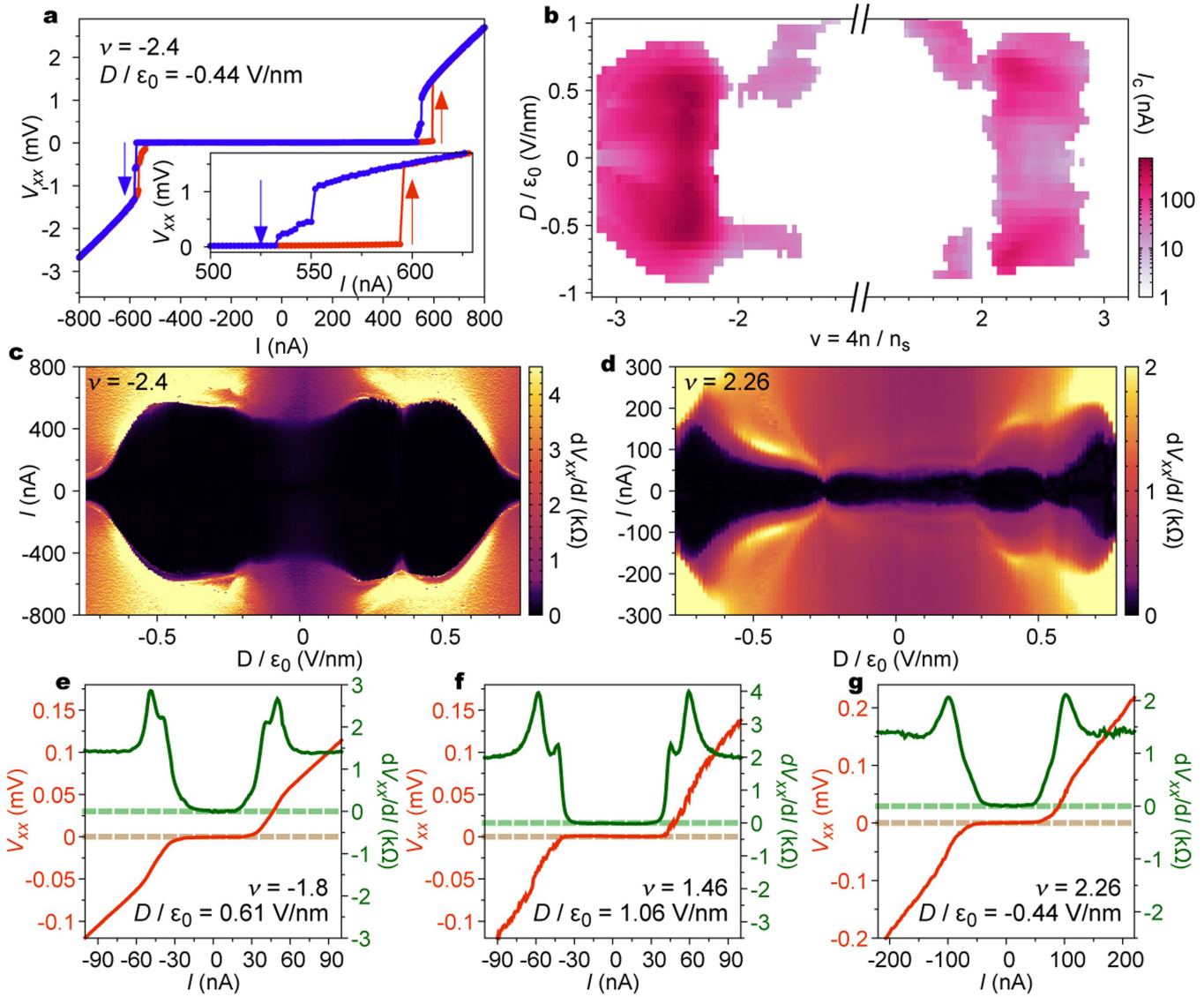

Extended Data Fig. 4 | V_{xx}–I curves and critical current I_c in MATTG. **a**, Forward (red) and backward (blue) sweeps of V_{xx}–I curves for the optimal point $\nu = -2.4$ and $D/\varepsilon_0 = -0.44$ V nm^{-1}. Inset, A clear hysteresis loop exists in the curve at $I \approx 550-600$ nA. **b**, Map of I_c versus ν and D in the major superconducting regions. **c**, Evolution of I_c over D at $\nu = -2.4$, showing that I_c initially increases as finite D is applied, and quickly decreases beyond local maxima near $|D|/\varepsilon_0 \approx 0.48$ V nm^{-1}. **d**, I_c versus D at $\nu = +2.26$ shows that the maximum I_c occurs near $|D|/\varepsilon_0 \approx 0.71$ V nm^{-1}, after which I_c quickly decreases. The modulation of superconducting strength in D may be due to change in the band flatness, as well as the interactions with the electrons in the Dirac bands. **e**–**g**, V_{xx}–I and dV_{xx}/dI–I curves for certain points in superconducting domes near $\nu = -2 + \delta$ (**e**), $\nu = +2 - \delta$ (**f**), and $\nu = +2 + \delta$ (**g**), all showing sharp peaks in dV_{xx}/dI at the critical current.

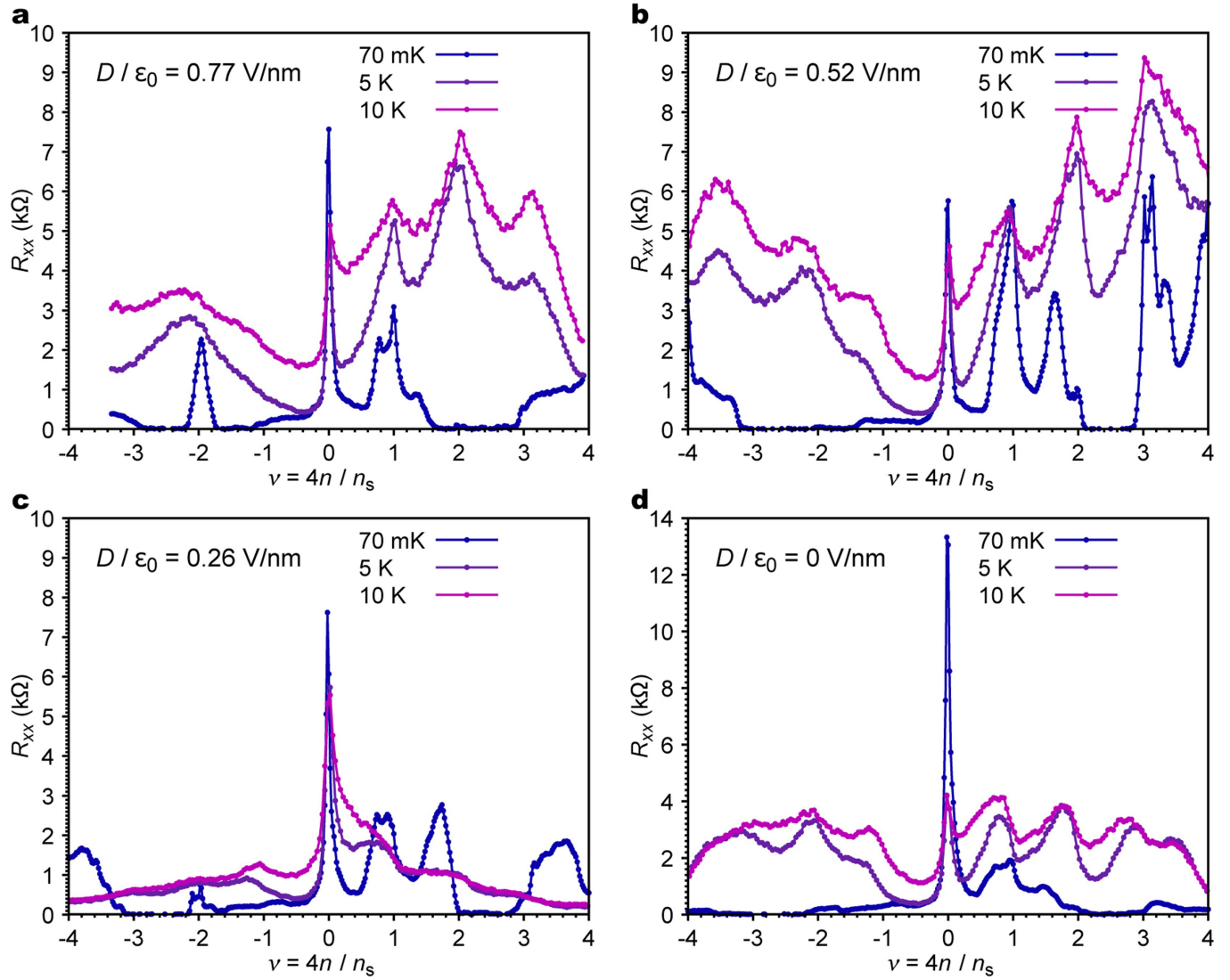

Extended Data Fig. 5 | R_{xx} versus ν at T = 70 mK, 5 K and 10 K. a–d, Measured at $D/\varepsilon_0 = 0.77\,\mathrm{V\,nm^{-1}}$ (**a**), $D/\varepsilon_0 = 0.52\,\mathrm{V\,nm^{-1}}$ (**b**), $D/\varepsilon_0 = 0.26\,\mathrm{V\,nm^{-1}}$ (**c**) and $D/\varepsilon_0 = 0\,\mathrm{V\,nm^{-1}}$ (**d**).

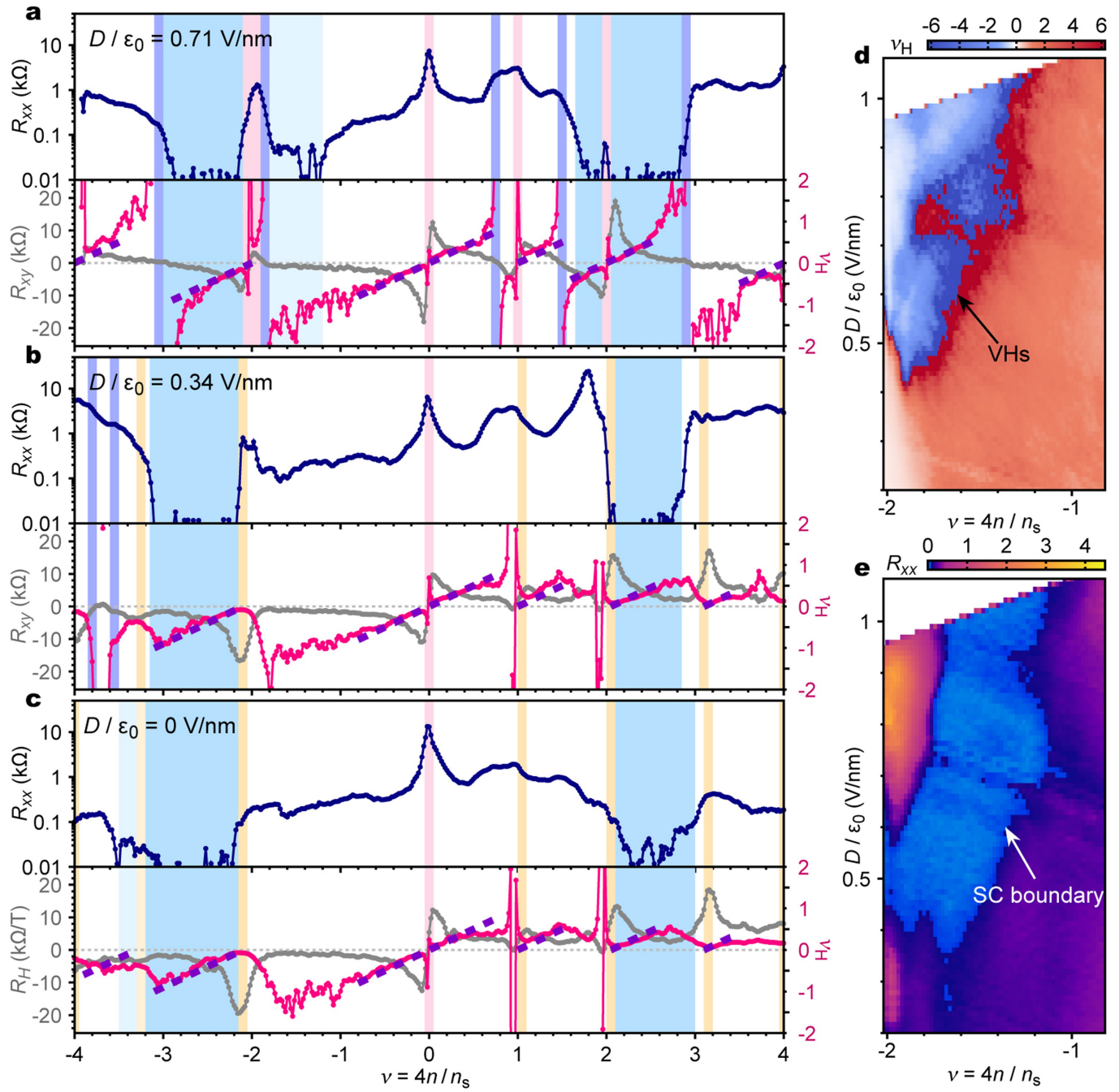

Extended Data Fig. 6 | Hall density analysis. a–**c**, Linecuts of R_{xx}, R_{xy} and ν_H (right axis) versus ν at representative D from high to zero, showing the bounding of major superconducting phases within the Hall density features. Vertical red, yellow, and dark blue bars denote 'gap/Dirac', 'reset' and 'VHS' features, respectively, and the light-blue regions denote superconductivity. Purple dashed lines show the expected Hall density. We note that there are some small regions right before $\nu = +1$ and $\nu = +2$ where for certain D values there are signatures of a more complex behaviour in ν_H, with VHSs possibly very close to the 'resets', as shown in Fig. 2b. **d**, The Hall density ν_H extracted from smaller magnetic fields of $B \approx 0.1$–0.3 T reveals a VHS boundary close to the weak superconducting phase boundary near $\nu = -2 + \delta$, which is absent in the Hall density shown in **a**–**c** and Fig. 2b extracted from a higher magnetic field of $B \approx -1.5$ T to 1.5 T. **e**, R_{xx} in the same region as shown in **d**, where the superconducting boundary is close to the VHSs. All measurements are performed at the base temperature $T \approx 70$ mK. SC, superconducting.

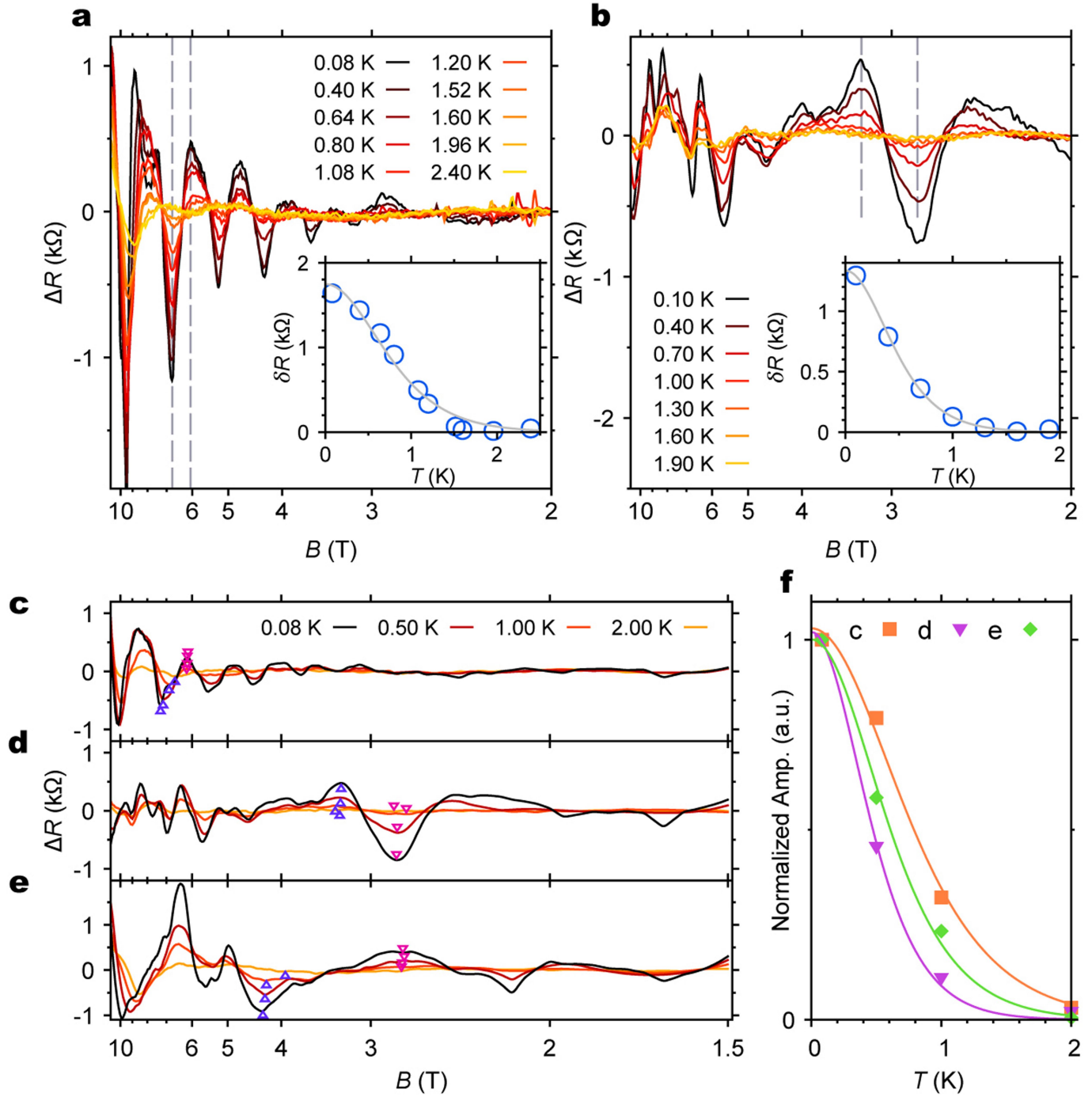

Extended Data Fig. 7 | Quantum oscillations and effective-mass analysis. All data shown here are measured at $D/\varepsilon_0 = -0.44$ V nm^{-1}. **a**, **b**, Quantum oscillations at $\nu = -2.86$ (**a**) and $\nu = -2.5$ (**b**) at different T. Grey dashed lines show the peaks used for analysis. Inset, Fit to the Lifshitz–Kosevich formula for the extraction of the effective mass, yielding $m^*/m_e = 1.25 \pm 0.13$ (**a**) and $m^*/m_e = 0.95 \pm 0.03$ (**b**). **c**, **d**, Quantum oscillations sampled at coarser points in T for the same ν as in **a**, **b**. Extracted effective-mass values with these coarser data are $m^*/m_e = 1.2 \pm 0.2$ (**c**) and $m^*/m_e = 0.96 \pm 0.09$ (**d**), matching the values from **a**, **b** within the uncertainty. **e**, Quantum oscillations at $\nu = -2.4$ (optimal doping). **f**, Lifshitz–Kosevich fits for the data shown in **c**–**e**, showing δR normalized with its value at the lowest temperature. The peaks chosen for extraction are marked with triangles in **c**–**e**. Amp., amplitude; a.u., arbitrary units.

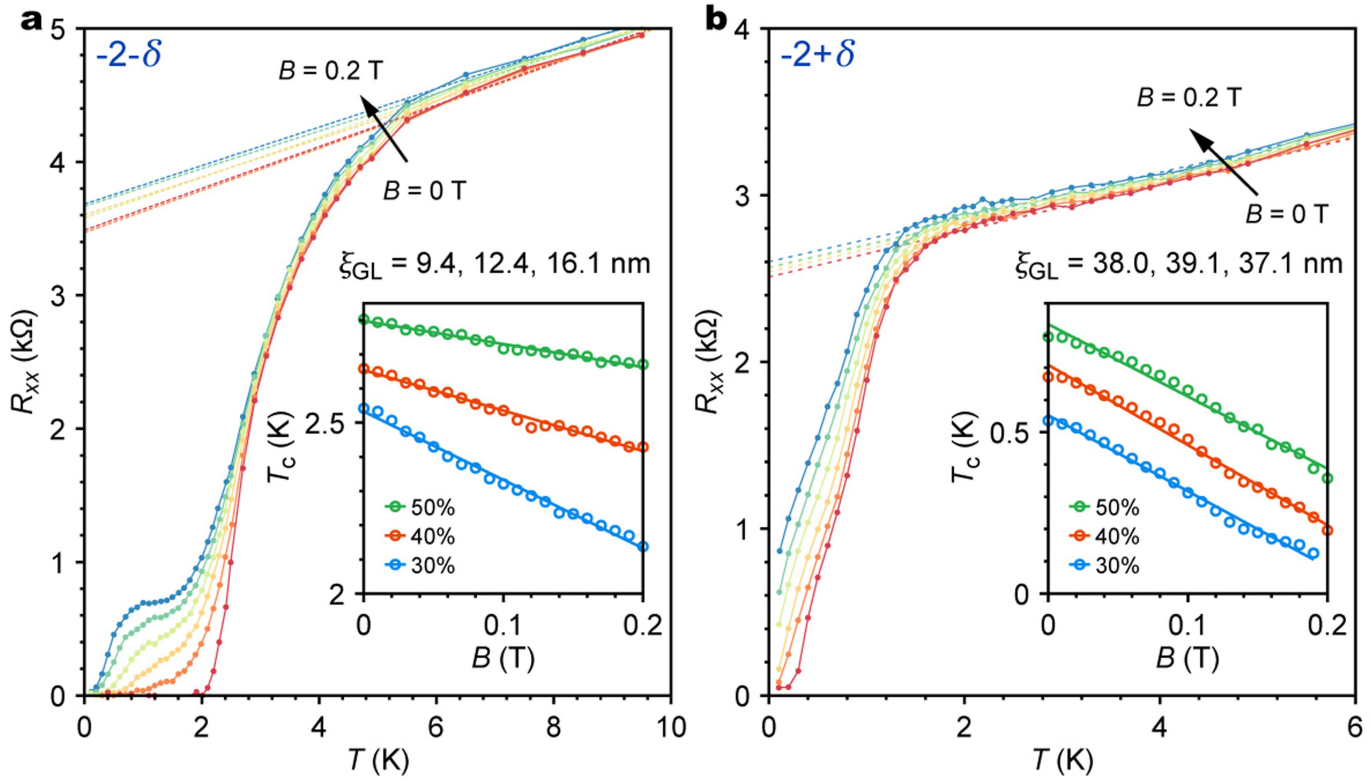

Extended Data Fig. 8 | Analysis of the Ginzburg-Landau coherence length. **a**, **b**, Superconducting transitions at perpendicular magnetic fields from $B = 0$ T to $B = 0.2$ T (40 mT between curves) for $\nu = -2 - \delta$ ($\nu = -2.4$; **a**) and $\nu = -2 + \delta$ ($\nu = -1.84$; **b**), from which the Ginzburg–Landau coherence length ξ_{GL} is extracted. $D/\varepsilon_0 = -0.44$ V nm^{-1} for both plots. Inset shows $T_c^{50\%}$, $T_c^{40\%}$ and $T_c^{30\%}$ as a function of B, from which we extracted the coherence length ξ_{GL} as 9.4 nm, 12.4 nm and 16.1 nm, respectively, for $\nu = -2 - \delta$. For $\nu = -2 + \delta$, we obtained 38.0 nm, 39.1 nm and 37.1 nm, respectively. We note that for $\nu = -2 - \delta$, the R_{xx}–T curves develop an extra transition ('knee') below T_c at finite B, which is possibly related to the melting transition between a vortex solid and a vortex liquid[48].

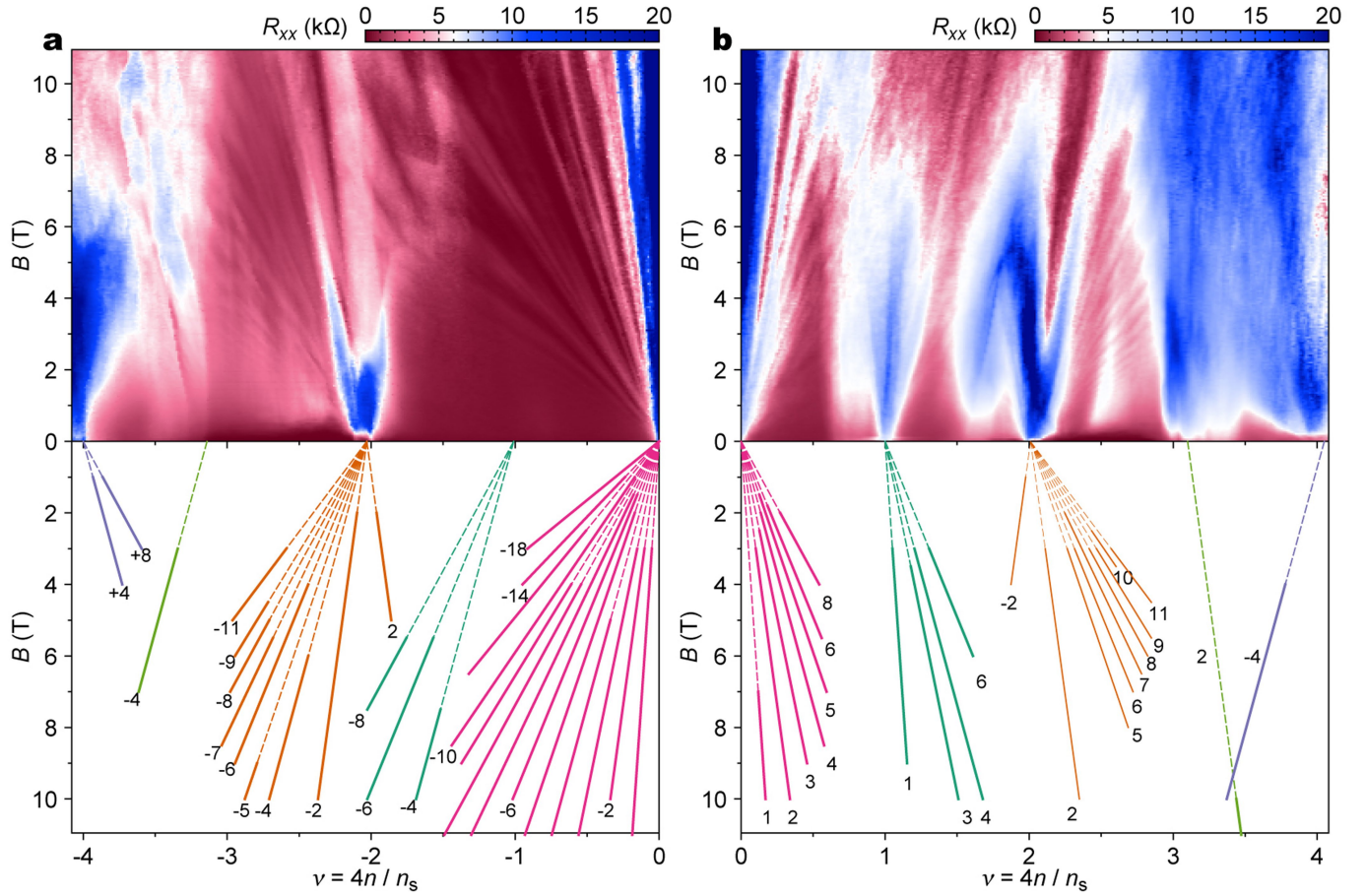

Extended Data Fig. 9 | Landau fans for intermediate *D*. **a**, **b**, Landau fans on the hole-doped (**a**) and electron-doped sides (**b**). They show the evolution between small D and large D, which exhibits a hybridization of the features. In **a**, the Landau fan diagram at $D/\varepsilon_0 = -0.34\ \mathrm{V\,nm^{-1}}$ for the hole-doped side shows the fans emanating from all integer fillings. An inward-facing fan from $\nu = -4$ starts developing, which meets the outward-facing fan from $\nu = -3$. Note also the appearance of an inward-facing fan from $\nu = -2$, which meets the outward-facing fan from $\nu = -1$. These observations agree with the formation of VHSs around these two regions in the intermediate $|D|$, where the electron-like carriers become hole-like, as illustrated in Fig. 4d, and identified in Fig. 2b. A small region of superconductivity starts appearing at $\nu = -2 + \delta$ while the carriers from $\nu = -2$ are present, as shown in Fig. 2a. In **b**, the Landau fan diagram at $D/\varepsilon_0 = -0.52\ \mathrm{V\,nm^{-1}}$ on the electron-doped side shows similar VHSs between $\nu \approx +1$–2 and $\nu \approx +3$–4. Similar to the hole-doped side, an inward-facing fan from $\nu = +2$ develops and meets with the outward-facing fan from $\nu = +1$. The density range of the inward-facing fan encompasses the appearance of a superconducting region at $\nu = -2 + \delta$ at this D.